REPORT DOCUMENTATION PAGE

AFRL-SR-AR-TR-02-

0407

Public reporting burden for this collection of information is estimated to average 1 hour per response, including the time for reviewing instruction data needed, and completing and reviewing this collection of information. Send comments regarding this burden estimate or any other aspect of this burden to Department of Defense, Washington Headquarters Services, Directorate for Information Operations and Reports (0704-0188), 12 4302. Respondents should be aware that notwithstanding any other provision of law, no person shall be subject to any penalty for failing to cor valid OMB control number. PLEASE DO NOT RETURN YOUR FORM TO THE ABOVE ADDRESS.

1. REPORT DATE (DD-MM-YYYY) July 29, 2002	2. REPORT TYPE FINAL TECHNICAL REPORT	3. DATES COVERED (From - To) 1 Apr 1998- 31 Dec 2001
4. TITLE AND SUBTITLE Advanced Coherent Transient Systems and Devices: Final Report		5a. CONTRACT NUMBER
		5b. GRANT NUMBER F49620-98-1-0283
		5c. PROGRAM ELEMENT NUMBER
6. AUTHOR(S) Wm. Randall Babbitt		5d. PROJECT NUMBER
		5e. TASK NUMBER
		5f. WORK UNIT NUMBER
7. PERFORMING ORGANIZATION NAME(S) AND ADDRESS(ES) Department of Physics Montana State University EPS Building Rm. 264 Bozeman, MT 59717-3840		8. PERFORMING ORGANIZATION REPORT NUMBER WRB02.01
9. SPONSORING / MONITORING AGENCY NAME(S) AND ADDRESS(ES) Air Force Office of Scientific Research/NE 801 North Randolph Street, Room 732 Arlington VA 22203-1977 Program Manager: Dr. Kent Miller Air Force Office of Scientific Research/NE		11. SPONSOR/MONITOR'S REPORT NUMBER(S)

20030107 035

12. DISTRIBUTION / AVAILABILITY STATEMENT
Approved for public release; distribution unlimited.

13. SUPPLEMENTARY NOTES
The views, opinions and/or findings contained in this report are those of the author(s) and should not be construed as an official Department of the Air Force position, policy or decision, unless so designated by other documentation.

14. ABSTRACT
The reported research explored non-traditional approaches to optical coherent transients applications and explored novel concepts designed to enhance optical coherent transient processing by exploiting the complex signal processing capabilities and non-linear behavior in optical coherent transient systems. The progress reported includes continuously programmed continuous processing optical coherent transient processor proposed and demonstrated; high efficiency echoes greater than 100% demonstrated; the theory and demonstration of the energy source of echoes; study of virtual echoes via a six wave mixing processes; BPSK and QPSK correlation demonstrating processing of multi-phase encoded information with optical coherent transient; nutational echoes investigated and demonstrated; new methods for multi-GHz pulse shaping and arbitrary waveform generation using optical coherent transients are proposed and proof-of-concept demonstration was performed; methods for obtaining high efficiency (58%) true-time-delay echoes using linear chirped programming are proposed; and optical control of geometric phase in an optical coherent transient system is experimentally demonstrated.

15. SUBJECT TERMS
Optical coherent transients, Spatial-spectral holography, Spectral holeburning, photons echoes, optical memory Optical correlation, Optical processing

16. SECURITY CLASSIFICATION OF:			17. LIMITATION OF ABSTRACT	18. NUMBER OF PAGES	19a. NAME OF RESPONSIBLE PERSON Wm. Randall Babbitt
a. REPORT UNCLASSIFIED	b. ABSTRACT UNCLASSIFIED	c. THIS PAGE UNCLASSIFIED	UL		19b. TELEPHONE NUMBER (Include area code) (406) 994-6156

Standard Form 298 (Rev. 8-98)
Prescribed by ANSI Std. Z39.18

Advanced Coherent Transient Systems and Devices

Final Report

for the period
3/1/98-12/31/01

Grant Number
F49620-98-1-0283

Sponsoring Scientific Office:

Air Force Office of Scientific Research/NE
801 North Randolph Street, Room 732
Arlington, VA 22203-1977

Prepared By

Wm. Randall Babbitt, Assoc. Prof.
Principal Investigator
Department of Physics
EPS Building 264
Montana State University
Bozeman, MT 59717-3840
(406) 994-6156

Executive Summary

The reported research explored non-traditional approaches to optical coherent transients (OCT) applications and explored novel concepts designed to enhance OCT processing by exploiting the complex signal processing capabilities and non-linear behavior in OCT systems. Here is a brief summary (by section) of the work performed and results obtained.

1. ___Continuously Programmed Continuous Processing___ A continuous OCT processor was proposed and demonstrated. Two spatially distinct programming beams continually write/refresh a spatial-spectral population grating, while a continuous input data stream generates a temporally overlapped, but spatially distinct, processed output signal. This system offers the ability to fully process a temporally structured waveform modulated in amplitude and phase at projected data rates greater than 10 GHz and with time-bandwidth products greater than 10,000.

2. ___High Efficiency Echoes___ In OCT systems, an important consideration is the recall efficiency. For photon echo memories, previously reported recall efficiencies were only a few percent. Here, methods of obtaining highly efficient (over 100%) data recall are proposed and demonstrated, both theoretically via simulation and experimentally.

3. ___Energy Sources of Echoes___ The mechanism leading to the coherent rephasing of the medium (echoes) has been well understood for many years, although there was considerable disagreement about the mechanism by which the stimulated photon echo (SPE) extracts its energy from the medium. Via simulation and experiment, it is shown that the energy of the SPE corresponds to a drop in the population of excited atoms at the time of the echo.

4. ___Study of Virtual Echoes___ Via a six wave mixing process, the non-casual virtual echo is rephrased and studied. The experimental and theoretical study explored the dynamics of the coherences that exist within the medium but don't rephase under typical echo sequences. These coherences can lead to non-linearities in more complex echo sequences.

5. ___BPSK and QPSK correlation___ Spatial-spectral holographic (SSH) devices are well suited to perform correlations with multi-phase encoded information. The operation of convolution and correlation are demonstrated with 30 symbol binary and quadrature phase-shift keyed (BPSK and QPSK) codes in Er:YSO at 1.5 micron.

6. ___Nutational Echoes___ Nutational behavior of echoes happens when the echoes are temporally longer than the delay and the Rabi oscillation period. Under these conditions, it was found that the echoes propagate in both causal and "non-causal" directions. These are new discoveries in the field and significant to understanding the physics of the optical coherent transients, especially in the understanding the continuous processing and efficient read-out.

7. ___Pulse Shaping Using Optical Coherent Transients___ Methods for multi-GHz pulse shaping and arbitrary waveform generation is proposed that uses chirped pulses that are controlled by low bandwidth electronics and acousto-optics. A proof-of-concept demonstration was performed.

8. ___High Efficiency True-time-delay Echoes Using Linear Chirped Programming___ Compared with the brief pulse programming of true-time-delays (TTD), it is found that linear frequency chirped TTD programming is significantly more efficient. It is found via simulation that echo power efficiencies can be as high as 58% under appropriately chosen conditions.

9. ___Control of Geometric Phase in OCT systems___ When a quantum system evolves along a cyclic route, it acquires a geometric phase. Geometric phase has been proposed as the means to prepare and control atomic qubits in quantum computation. An experimental demonstration of the optical control and detection of the geometric phase with OCTs in Barium vapor is reported.

___Personnel and publications___ The grant funded (in-part or wholly) 3 post-doctoral, 5 graduate, and 2 undergraduate students, 4 theses, 12 journal papers, 40 presentations, and a patent filing.

Project Objectives

The main objective of the proposed research was to advance beyond the traditional implementations and applications of coherent transients and to explore novel concepts that exploit the processing and non-linear behaviors of coherent transient systems. These areas included 1) Energy source of photon echoes, 2) continuously programmed continuous processor, 3) efficient writing and reading 4) feedback and learning, 5) inversion and gain gratings, 6) index modulation, 7) single sideband and frequency modulation, and 8) bilinear transforms and circuit modeling. The proposed research also explored critical issues that significantly impact the development of practical coherent transient systems. These include: 1) orthogonal code development 2) modeling and characterization of gated systems, and 3) cryocooler evaluation.

As part of understanding of physics of coherent transient formation, we have also investigated the phenomena of virtual echoes and the nutational behavior of quasi-continuous echoes. We also have studied geometric phase control of optical coherent transients in Barium vapor. Understanding of these aspects has aided in the understanding of the energy sources of echoes, efficient writing of echoes, continuous reading and the effects of index modulation on echoes.

Achievements/New Findings

1. *Continuously Programmed Continuous Processing*

Optical coherent transient (OCT) devices such as an optical memory[1], optical signal cross-correlator[1-3], and optical true-time delay regenerator[1,2] have been proposed and demonstrated. While each device has different aspects in its programming and processing stages, all are implementations of a generalized OCT processor. A continuous OCT processor has been proposed[3] and demonstrated[4]. By using two spatially distinct programming beams to write a spatial-spectral population grating, the emitted output signal is spatially distinct from the subsequently applied continuous input data stream, and thus can temporally overlap it. This system offers the ability to fully process a temporally structured waveform (TSW) modulated in amplitude and phase at projected data rates greater than 10 GHz and with time-bandwidth products greater than 10,000[4].

OCT devices can only process data as long as the programmed spatial-spectral grating survives. When the programming stage is a single shot event, writing a strong spectral grating in a non-persistent hole-burning material, the processing stage can occur until the excited absorbers decay to their ground states. After the grating decays away fully, the programming stage can be repeated, but this leads to dead time for the processor, several times the excited state lifetime T_1. An alternative implementation is to utilize persistent spectral holes. But for single photon persistent holes (e.g., hyperfine storage), the processing stage is partially destructive to the stored grating[4]. For two-photon persistent holes (i.e., gated storage),[1] the processing stage is non-destructive and can be continuous[3], but low writing and gating efficiencies of available materials make this currently impractical. Each of the above techniques requires strong programming pulses, a disadvantage that could be lessened if the grating were accumulated by repeating the programming and gating processes. However, the temporal distinction between the programming and processing stages still remains for all the above techniques, along with the constraints on efficiency, materials, and devices.

In this project, we proposed a method for achieving continuous processing in materials that do not exhibit long-term persistent hole burning. Efficient and continuous processing can be accomplished between the upper and lower levels of a non-persistent inhomogeneously broadened transition (IBT). The stored grating is accumulated and refreshed by repeatedly applying the programming sequence[2]. The input beam geometry isolates the emitted signal from all the input waveforms, so that the optical signal processor can simultaneously, asynchronously, and continuously process an input signal while it is being continuously programmed.

In general, an OCT processor is programmed with two temporally modulated optical pulses that are separated in time and resonant with an IBT. Each laser pulse has a form $E_n(t - t_n - \eta_n) \cos(\omega_0(t - \eta_n) + \phi_n)$, where the n subscript determines the order of arrival of each pulse, $E_n(\tau)$ is a slowly varying temporal envelope function, ω_0 is the laser center frequency, $\eta_n = (\hat{k}_n \cdot \vec{r} / c)$, where $\hat{k}_n$ is the unit wavevector of pulse n, ϕ_n is the phase of pulse n, and each pulse reaches the medium at $\vec{r} = 0$ at its arrival time t_n. The two waveform envelopes $E_1(\tau)$ and $E_2(\tau)$, separated by $\tau_{21} = t_2 - t_1$, write a spatial-spectral holographic population grating on the IBT. A programming pulse can be a temporally brief reference pulse (BRP), a linear frequency-chirped reference pulse, or a TSW comprised of individual sub-pulses that represent data.

After a grating is programmed, the atomic absorption is selective in both frequency and space for subsequently applied optical waveforms. Within the grating lifetime, a subsequently applied $E_3(\tau)$ causes a coherent emission $E_S(t - t_S - \eta_S)\cos(\omega_0(t - \eta_S) + \phi_S)$ from the IBT with the temporal envelope of the form

$$E_S(t - t_S - \eta_S) \propto \int_{-\infty}^{\infty} E_1^*(\Omega)E_2(\Omega)E_3(\Omega)e^{i\Omega(t - t_S - \eta_S)}d\Omega, \qquad (1\text{-}1)$$

where $t_S = t_3 + t_2 - t_1$, $\eta_S = \eta_3 + \eta_2 - \eta_1$, $\phi_S = \phi_3 + \phi_2 - \phi_1$, and $E_n(\Omega)$ is the Fourier transform of the nth applied optical waveform envelope, $E_n(\tau)$. Equation (1-1) is based on the Fourier Transform approximation of the input temporal waveforms[1,2], valid for waveforms with bandwidths less than the inhomogeneous linewidth, $\delta\omega_I$, and intensities that insure a linear response, avoiding both coherent and incoherent saturation[3].

The phase matching condition for the proposed continuous processing and programming technique is $\hat{k}_S = \hat{k}_3 + \hat{k}_2 - \hat{k}_1$, where all three input pulses are distinct such that $\hat{k}_1 \neq \hat{k}_2 \neq \hat{k}_3$. Figure 1-1(a) shows a three-dimensional representation of this scheme. Perfect phase matching is achieved if the pulses are directed such that for a given vector $\vec{k}_0$, the individual wavevectors are $\hat{k}_n = \vec{k}_0 + \delta\vec{k}_n$, where for n=1,2,3, every $|\delta\vec{k}_n|$ is equal, $\delta\vec{k}_n \perp \vec{k}_0$, and $\delta\vec{k}_3 = -\delta\vec{k}_2$. In addition, phase-matched angular multiplexing is achieved by varying $\delta\vec{k}_1$ while maintaining the above conditions.

The complete spatial-temporal implementation of the input pulses is shown in Figure 1-1(b), for the specific case of a signal cross-correlator. In this schematic, a pair of programming pulses $E_1^{(j)}(\tau)$ and $E_2^{(j)}(\tau)$ is repeated at regular intervals τ_R. In this case, the first (second) programming pulse is a TSW (BRP) on beam 1 (beam 2). Once the grating is accumulated, the waveform to be processed can be propagated along beam 3. Here, the programmed pattern is included twice in this waveform. Figure 1-1(c) shows

the shape and timing of the resulting output signal emitted along $\hat{k}_S$, with respect to the third pulse after it exits the medium. Here, this signal consists of two auto-correlation peaks and other correlation signals, provided the accumulated grating does not saturate and distort.

Certain conditions must be satisfied to obtain efficient processing. First, consider the programming timing limitations with respect to material parameters. We define a generalized three-level system where the radiation field only couples states $|1\rangle$ and $|2\rangle$ and there is an intermediate state $|3\rangle$, with population relaxation times κ_{21}^{-1}, κ_{23}^{-1} and κ_{31}^{-1} between the numbered states. This reduces to a two-level system if $\kappa_{23}=0$. The upper and intermediate state lifetimes are $T_1 = (\kappa_{21}+\kappa_{23})^{-1}$ and $T_B = \kappa_{31}^{-1}$. In general, the quantity $(\tau_{21}+\delta\tau_1+\delta\tau_2)$ is limited by the homogeneous dephasing time T_2. The inclusion of the pulse duration $\delta\tau_n$ of pulses 1 and 2 accounts for the general case when $\delta\tau_n \ll \tau_{21}$ is not satisfied. Requiring $T_2 \geq 40(\tau_{21}+\delta\tau_1+\delta\tau_2)$ makes the loss of efficiency due to coherent decay less than 10%, although techniques exist to compensate for this loss.[2] Setting $\tau_R \geq 2T_2$ avoids coherent interference between successive pairs of programming pulses. Setting τ_R much less than the greater of T_1 or T_B insures that the repeated programming pulse pairs at the appropriate intensity form an accumulated grating[8], where after reaching steady state, their application exactly compensates for the relaxation losses during τ_R. The relaxation losses during τ_R cause a fractional drop in the intensity of the output signal, ε. For ε to be small, τ_R must be chosen appropriately.

Beyond the population decay dynamics, the stability of the optical source is an important consideration, analogous to the discussion in Ref. 3. In practice, each repeated programming sequence may not be identical. The stored grating from a single pair of programming pulses, $G(\Omega) \propto E_1^*(\Omega)E_2(\Omega)e^{i(\Omega\tau_{21}+\phi_{21})}+c.c.$, depends on the phase difference $\phi_{21} = \phi_2 - \phi_1$ between the two pulses. This phase difference can fluctuate due to short-term frequency drift of the optical carrier. If the carrier frequency changes to $(\omega_0 + \delta\omega_0)$, a change in the phase difference between the programming pulses of $\delta\phi_{21} = \delta\omega_0 \cdot \tau_{21}$ will result. Consider any two programming pulse pairs, labeled the j-th and k-th pairs, that occur within a time shorter than T_B. If $\phi_{21}^{(k)}$ differs from $\phi_{21}^{(j)}$ by roughly π, then the pulse pairs contribution leads to incoherent accumulation of the grating and ineffective processing. The requirement exists, therefore, that $(\phi_{21}^{(k)} - \phi_{21}^{(j)}) \ll \pi$, implying that the short-term laser frequency stability should follow $\delta\omega_0 \ll \pi/(\tau_{21} + \delta\tau_1 + \delta\tau_2)$ over any time period T_B. When a single optical source creates the programming and processing beams, its long-term frequency drift is inconsequential, provided all pulse bandwidths stay well within $\delta\omega_I$. As the laser drifts, the previous grating decays and the new grating seamlessly accumulates when the above condition is maintained.

Assuming a stable optical source, a continuously programmed continuous processor has the ability to produce a highly efficient grating. For continuously programmed memories and processors, when pulse 1 or 2 is a TSW, optimizing the efficiency must be balanced with non-linearities that lead to signal distortion. But for the case of a true-time delay device when the first two pulses are both BRP's, the efficiency analysis follows from the treatment of accumulated gratings in Ref. 8, where the steady state population

solutions are derived for a three level system. For an absorber at frequency ω, the steady-state spectral population difference between the excited and ground states is

$$w(\Delta) = (1-p)\frac{e^{-x_1}(1-e^{-x_B}) + \beta(e^{-x_B} - e^{-x_1})/2}{1 - e^{-x_B} - pe^{-x_1}(1-e^{-x_B}) + \beta(1-p)(e^{-x_B} - e^{-x_1})/2} - 1, \qquad (1\text{-}2)$$

where $\Delta = \omega - \omega_0$, $\beta = \kappa_{23}/(\kappa_{23} + \kappa_{21} - \kappa_{31})$, $x_B = \tau_R/T_B$, $x_1 = \tau_R/T_1$, and $p = 1 - 2\theta^2 \cos^2(\Delta\tau_{21}/2 + \phi_{21})$ assuming that $\theta_1 = \theta_2 = \theta$, where θ_n is the area of pulse n, $\theta \le 0.1\pi$ and $\tau_{21} \ll T_2$. Equation 1-2 reduces to the two-level case when $\beta = 0$.

A qualitative estimate of the intensity of the true-time delay output signal is the magnitude squared of the inverse Fourier Transform of Eq.(1-2), evaluated at τ_{21}. For reference, the efficiency is normalized against that of a photon-gated two-level persistent holeburning system with gating efficiency, γ_{gate}, equal to one3. In general, given fixed values for T_1, T_B and β, the efficiency can be optimized to η_{opt} for any given τ_R by varying θ to a value θ_{opt}. Increasing τ_R increases both θ_{opt} and ε. It is found that η_{opt} is identical for all τ_R and $\eta_{opt} = 0.47$. Thus, non-persistent materials can have efficiencies higher than a photon-gated material with $\gamma_{gate} < 0.68$, since the output intensities of gated systems go as γ_{gate}^2. Currently available gated materials have $\gamma_{gate} \ll 1$[7], so in comparison to these the efficiency of a continuously programmed grating is several orders of magnitude greater. For $T_B \gg T_1$, the efficiency is due almost entirely to the first harmonic of the accumulated grating in the ground state, not the upper state. For $\beta=0$ or for $T_B \ll T_1$, both ground and upper state population gratings contribute to the efficiency.

Consider two non-persistent material systems that are currently available and at wavelengths compatible with commercially available diode lasers. For a three-level system, Tm^{3+}:YAG (0.1 at. %) offers an intermediate bottleneck level between the two-level IBT at 793 nm. At 4.4 K, $\delta\omega_I \sim 17$ GHz, $T_2 \sim 16$ μs, $T_1 \sim 800$ μs, $T_B \sim 9$ ms, and $\beta = 0.59$.[4,6] Setting τ_R=32 μs yields θ_{opt}=0.05π and ε=2.0%. Delays up to 0.4 μs are feasible without any compensation[9,] provided the laser frequency is stable to 250 kHz over 10 ms. For a two-level system, Er^{3+}:LiNbO$_3$ (0.06 at. %) has an IBT at 1.53 μm. At 1.6 K, $\delta\omega_I \sim 200$ GHz, T_1=10 ms (β=0), and T_2=40 μs in a 3 kGs external magnetic field.[6] Setting τ_R=80 μs yields θ_{opt}=0.045π and ε=1.6%. Delays up to 1.0 μs[9] are feasible for a laser stable to 100 kHz over 10 ms. For both cases, the efficiencies are still better than a gated material with $\gamma_{gate} < 0.68$.

This analysis and predicted efficiencies are valid for the OCT true-time delay regenerator[5] programmed with BRP's as well as with frequency chirped reference pulses.[6] The input beam geometry has the benefit that non-linearities introduced by the multiple programming stages do not lead to harmonics of the delay in the output signal direction in the case of true time delay regenerators.

In summary, we have proposed a novel OCT technique for programming and processing. Utilizing distinct processing and programming beams makes it possible to simultaneously program a grating while asynchronously processing a continuous waveform against it. New delays or patterns can be reprogrammed into the material in a time roughly equal to the greater of T_B or T_1. This technique alleviates the need for photon gating in several types of OCT devices, specifically optical DRAM, temporally

5

structured waveform cross-correlators, and true-time delay regenerators. Multi-gigahertz, efficient, real-time processing with large time bandwidth products (>10,000) can be achieved in currently available non-persistent materials.

References for section 1

[1] T. W. Mossberg, *Opt. Lett.* **7,** 77 (1982)

[2] Y. S. Bai, W. R. Babbitt, N. W. Carlson and T. W. Mossberg, *Appl. Phys. Lett.* **45,** 714 (1984)

[3] W. R. Babbitt and J. A. Bell, *Appl. Opt.* **33,** 1538 (1994)

[4] M. Zhu, W. R. Babbitt and C. M. Jefferson, *Opt. Lett.* **20,** 2514 (1995)

[5] K. D. Merkel and W. R. Babbitt, *Opt. Lett.* **21,** 1102 (1996)

[6] K. D. Merkel and W. R. Babbitt, *Opt. Lett.* **23,** 528 (1998)

[7] W. E. Moerner, Editor. Persistent Spectral Holeburning: Science and Applications, Topics in Current Physics, Vol. 44 (Springer-Verlag, Berlin, 1988), and references therein.

[8] W. H. Hesselink and D. A. Wiersma, *J. Chem. Phys.* **75,** 4192 (1981)

[9] K. D. Merkel and W. R. Babbitt, *Opt. Comm.* 128, 136 (1996)

[10] U. Elman, B. Luo, S. Kroll, *J. Opt. Soc. Am. B* **9,** 1905 (1996)

[11] J. A. Caird, L. G. Deshazer and J. Nella, *IEEE J. Quantum. Electron.* **QE-11,** 874 (1975)

[12] R. M. Macfarlane, *Opt. Lett.* **18,** 1958 (1993)
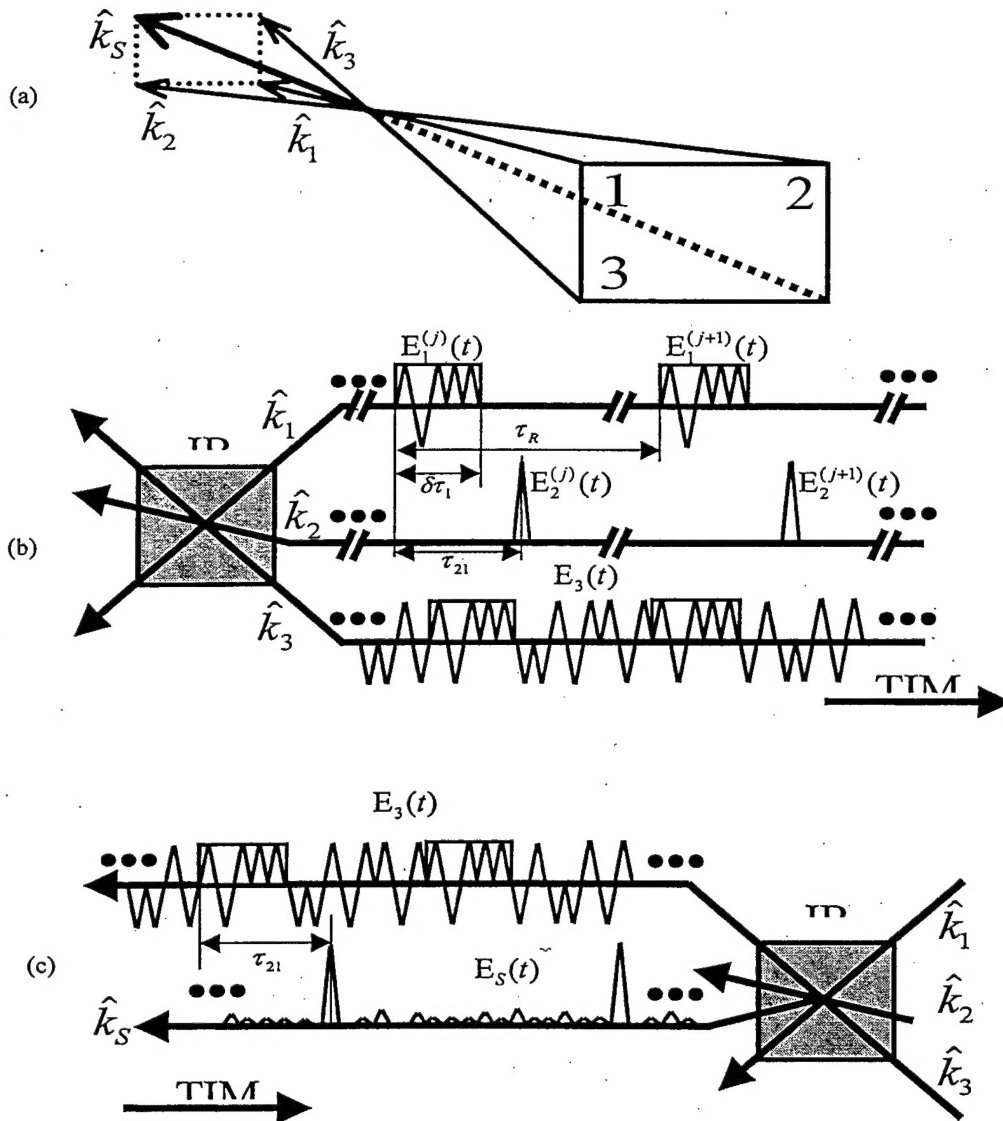
[13] Y. Sun, Private communication.

Fig. 1-1. (a) Perfect phase matching geometry for three distinct input beams, and direction of the emitted output signal $\hat{k}_S$. (b) Schematic of a continuously programmed continuous processor, and parameters, as a signal cross-correlator. Pairs of programming pulses are repeated along beams 1 and 2 to accumulate a grating. In any pair, pulse 1, on beam 1, is a pattern waveform that interferes with pulse 2, on beam 2, a brief reference pulse. Once the grating is accumulated, a continuous waveform to be processed is introduced along beam 3. (c) Schematic of the emitted output signal due to the inputs in (b) shown in relation to the waveform on beam 3 after the IBA. Outputs along beams 1 and 2 are not shown.

2. *High Efficiency Echoes*

Optical coherent transients offer advantages over their electronic counterparts for a variety of high bandwidth applications including memory systems, signal processors, routers, and true time delay.[1-4] In these systems, an important consideration is the recall efficiency, which can affect the information storage capacity, and the overall complexity of the system. For photon echo memory storage of a sequence of optical data bits is stored in an inhomogeneously broadened medium with the additional application of

temporally brief reference pulses that initiate the storage or recall processes. A reference pulse is considered brief if it is less than one-third of the time duration of a data bit. Each data bit is relatively weak (typically much less than 0.1π pulse area) compared to the reference pulse, and the medium responds to it in a linear fashion. Directly measured efficiencies greater than 100% are particularly interesting because they open the possibilities of cascaded devices and gain in feedback (adaptive learning) systems.

The recall power efficiency of the waveform is determined by dividing the peak power of a recalled bit by the peak power of the input data bit. The recall power efficiency can be slightly different from the energy efficiencies if the temporal shape of the data is not recalled identically. In this Letter, unless specifically stated otherwise, the term efficiency will refer to the recall power efficiency defined above. Achieving greater than unity efficiency does not imply a violation of conservation of energy. During the recording and read out process, energy from the brief reference pulses is stored in the atomic population and extracted by the echo.

We have shown through numerical simulations of the Maxwell-Bloch equations that highly efficient recall of modulated waveforms is possible in absorbing media, with recall efficiencies greater than 250% for two pulse echoes (2PE) and greater than 225% for stimulated photon echoes (SPE). These high recall efficiencies are predicted for plane wave illumination of optically thick media (absorption lengths ranging between 3.5 to 4.5) combined with brief pulse areas ranging between 0.7π to 0.9π. Further, the recalled temporal waveform exhibits good signal fidelity under the conditions for which the highest efficiency is achieved. Experiments in gaseous media have shown directly measured photon echo power efficiencies up to 25% for absorption lengths less than 3, with material relaxation corrected efficiencies up to 170% for the 2PE and 70% for the SPE.[5-7] However, in this project we experimentally demonstrate recalled waveform efficiencies up to 235% for the 2PE, and up to 150% for the SPE. The reported efficiencies are direct measurements, and have not been adjusted to account for material relaxation, spectral diffusion, or beam profile. To the best of our knowledge, this is the first demonstration of uncorrected efficiencies greater than 100% using a single pass configuration (without amplification)[8] in an optically thick medium.

The excitation source for the experiment was a frequency-stabilized cw Ti:Sapphire laser operating at 1.5 watts and tuned to 793 nm, resonant with the $^3H_6 \leftrightarrow {}^3H_4$ transition of Tm^{3+}:YAG. The pulse sequences used for the experiments were generated with an acousto-optic modulator (AOM) driven by an arbitrary waveform generator that deflected the pulses from the main beam. The shape of the brief pulses had a non-negligible effect on recall efficiencies, particularly for the 2PE. The maximum efficiency was obtained when the brief pulses had rounded temporal shapes for the SPE sequences and roughly square temporal shapes for the 2PE sequences. All data pulses had roughly square temporal shapes. The deflected beam passed through a half-wave plate for polarization control and was then focussed into a Tm^{3+}:YAG crystal mounted inside a cryostat. The crystal was 2 cm long, with an absorption length of approximately 3.8 ± 0.1 and a measured homogeneous lifetime of 85 μsec at 3.9 Kelvin. The brief reference pulses and the data pulses were extracted from the same laser beam, were collinear, and had spatial gaussian profiles. The pulse areas given in this paper describe the response of the system to the center of the beam. However, for a gaussian spatial profile, the major contribution comes from a ring around the center of the beam. Thus the response of the medium to a

pulse of *given* area θ is closer to a theoretical response of a plane wave pulse with *smaller* pulse area. All input pulses were focused to a beam waist of ~ 70 μm inside the crystal, with a Rayleigh range of 1.4 cm. Although it would have been advantageous to have the waist of the reference beam larger than the data beam, this configuration was not possible due to the power limitations of the laser, and the need to propagate through a 2 cm crystal. The crystal was oriented such that ``single dipole'' interaction was observed with the optical field propagating along the < 110 > direction with polarization along the [111] direction.[9] A pick-off mirror was placed before the cryostat and deflected 10% of the beam onto a reference photodetector (PD_{in}), while the output from the cryostat was measured with a second photodetector (PD_{out}). The ratio PD_{out}/PD_{in} was measured while the laser was tuned off resonance. When on resonance, PD_{in} was multiplied by this ratio to determine the input sequence power as it would have been measured after the cryostat *off resonance*. This enabled real time monitoring of the input beam and provided an accurate method of determining the recall efficiency. All signals were captured with a digitizing oscilloscope.

Figure 2-1 shows a photon echo for a two-pulse input sequence. The dotted line represents the input sequence as measured after the crystal and with the laser tuned off resonance. The solid line shows the response of the system to the input sequence when the laser is tuned to the center of the absorption curve. The first pulse is weak with a pulse area $\theta_{data} = 0.18\pi$ and a pulse duration $\tau_{data} = 700$ nsec. The second pulse is temporally brief with $\theta_{brief} = \pi$ and $\tau_{brief} = 135$ nsec. The delay between the centers of the two pulses τ_{21} was 1.38 μsec. The photon echo had a rounded temporal profile with a full width half maximum (FWHM) of 500 nsec. It is important to note that the 235% power efficiency is an uncorrected measurement. If we take into account the echo reduction due to the homogeneous lifetime, the recall efficiency would have been 250%. The theoretical efficiency for a plane wave propagation of this pulse sequence is ~ 500%. It was observed that for 2PE's, as the brief pulse area was increased, the experimental recall efficiency differed from the theoretical efficiency, up to a factor of 2. We believe that the reduced efficiency is most likely due to the Gaussian spatial profile of the laser beam which results in a distribution of brief pulse areas and thus the data beam experiences different efficiencies across its spatial profile.

In Figure 2-2(a) we show the input data sequence with bit pattern (-1,0,1,1,0,-1,0,-1,1). For each bit, $\tau_{bit} = 600$ nsec, $\theta_{bit} = 0.1\pi$, and the distance between adjacent bit centers $\tau_{bb} = 880$ nsec so the optical power returns to zero between adjacent bits. The brief pulse parameters were identical to the previous case. In Figure 2-2(b) the brief pulse and recalled bit sequence are shown. The recalled waveform, in the case of a two-pulse echo, is a time-reversed replica of the input data sequence. The recall efficiency for the sequence ranged between 70% for bit 1, up to 235% for bit 5. The individual bit efficiencies show a general exponential decay that is typical for the lifetime of the material, along with the influence of two-pulse and stimulated echoes from interactions other than the desired 2PE's that come directly from a single bit and brief pulse combination. Specifically, bit 4 was reduced and bit 5 was slightly enhanced by the destructive and constructive interference of other echoes. However, bit 5 would still have exhibited > 200% efficiency without the enhancement. If the material relaxation is taken into account, bit 1 had an efficiency of 110% and the highest bit efficiency, bit 5, was 255%. The recalled data bits had excellent signal contrast, with a return to zero between

9

adjacent bits. In fact, the experimental recall process exhibits better signal fidelity-and narrower echoes-than the numerical simulation results in which the echoes broaden and show distortion when $\theta_{brief} > 0.8\pi$.

The stimulated photon echo (SPE) is employed to achieve storage times much longer than the tens of microseconds limit typical of homogeneous decay and to obtain a time-forward replica of the stored information. For the SPE, a brief write pulse followed by a data sequence forms a spectral population grating. For both brief pulses, $\tau_{brief} = 135$ nsec. Within the lifetime of the grating, a second brief pulse initiates the recall process. In Fig. 3, the SPE is shown (solid line) for an off resonance sequence (dotted line) with a single weak data pulse where $\theta_{data} = 0.15\pi$ and $\tau_{data} = 700$ nsec. A maximum SPE with efficiency 150% was obtained when the brief pulses had identical pulse areas of 0.9π. The energy efficiency of the SPE was 100%. The maximum theoretical plane wave recall efficiency was 225% for $\theta_{brief} = 0.7\pi$.

Figure 2-4 shows a recording of a SPE for a (1,-1,0,1) bit sequence. The brief pulse parameters were identical to those in Fig. 3. The data bit parameters were $\theta_{bit} = 0.07\pi$ and $\tau_{bit} = 440$ nsec, with $\tau_{bb} = 880$ nsec. The distance between the first brief pulse and the first (third) bit was 1.00 (3.64) μsec. The second brief pulse occurred roughly 70 μsec after the first brief pulse, well within the 800 μsec upper state lifetime. The directly measured recall efficiency for each ±1 bit in the sequence was 115%, 148%, and 80% respectively. The efficiencies, when corrected for relaxation, were 120%, 161%, and 95%, respectively. The larger efficiency for the second bit reflects the presence of a two-pulse echo resulting from the second brief pulse and the first stimulated echo.

In conclusion, we have presented the first observation, to the best of our knowledge, of two-pulse and stimulated photon echoes with directly measured recall power and energy efficiencies greater than 100%. The experimental results demonstrate that highly efficient waveform recall is achievable in optically thick media. Further, the data clearly show that signal fidelity is not significantly compromised under those conditions in which maximum echo efficiency is observed. Photon echo efficiencies up to 235% were directly measured. These results are important in that they significantly affect the feasibility of photon echo applications such as memory systems, signal processors, routers and true time delay as well as cascaded systems, and systems with optical feedback.

References for Section 2
[1] T. W. Mossberg, Optics. Lett. **7**, 77 (1982).
[2] W. R. Babbitt and J. A. Bell, Applied Opt. **33**, 1538 (1994).
[3] W. R. Babbitt and T. W. Mossberg, Optics Lett. **20**, 910 (1995).
[4] K. D. Merkel and W. R. Babbitt, Optics Lett. **21**, 1102 (1996).
[5] M. Azadeh, C. Sjaarda Cornish, W. R. Babbitt, and L. Tsang, Phys. Rev. A **57**, 4662 (1998).
[6] C. Sjaarda Cornish, M. Azadeh, W. R. Babbitt, and L. Tsang, *Proc. of the SPIE*, Vol. 3468, 174(1998).

[7] T. Wang, C. Greiner, J. R. Bochinski, and T. W. Mossberg, Phys. Rev. **A** 60, R757 (1999).

[8] K. R. Mohan, U. Elfman, M. Tian, and S. Kroll, Optics Lett. 24, 37-9 (1999).

[9] C. Greiner, B. Boggs, T. Loftus, T. Wang, and T. W. Mossberg, Phys. Rev. A 60, R2657 (1999).
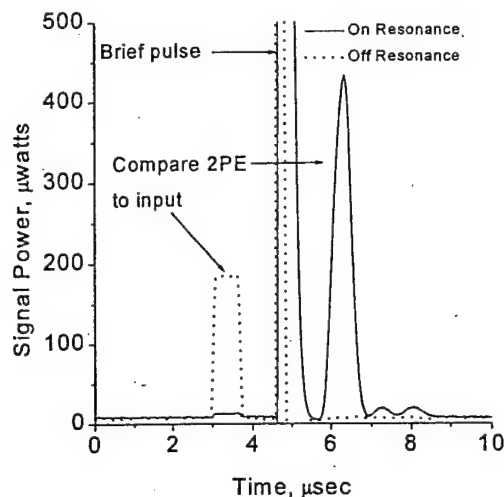
Fig. 2-1 Two pulse photon echo for a single weak data pulse. The dotted line represents the input sequence as measured after the crystal while off resonance. The solid line represents the output from the crystal on resonance. The 2 pulse echo has a recall power efficiency of 235%.
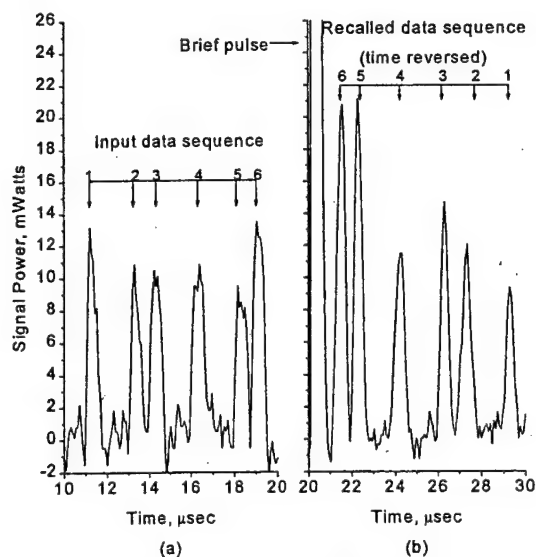

Fig. 2-2 Two pulse photon echoes showing the recall efficiency of a data sequence. The input bit sequence is shown on the left and the recalled data sequence is on the right. The input bit pattern was (-1,0,1,1,0,-1,0,-1,1). The recall efficiencies range between 70% for bit 1, up to 235% for bit 5.
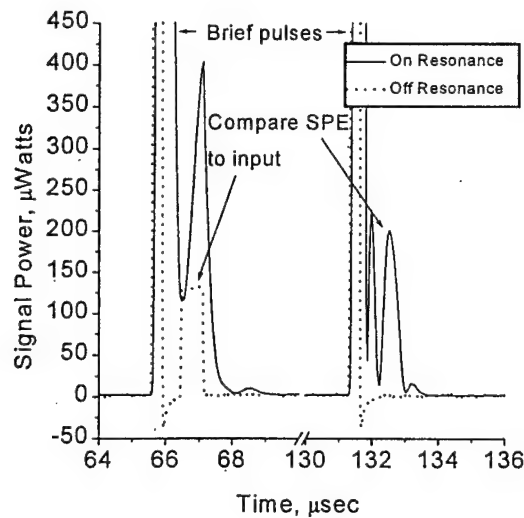
11

Fig. 2-3 Stimulated photon echo for a single weak data pulse. The dotted line represents the off resonance sequence and the solid line represents the on resonance output from the crystal. The SPE has a recall power efficiency of 150%.
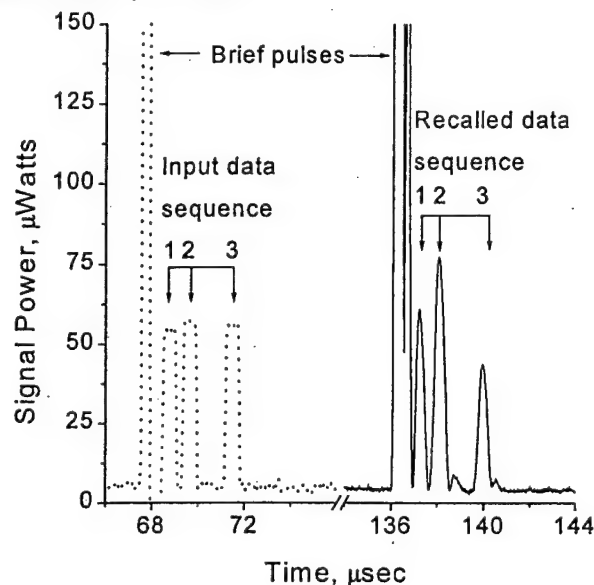

Fig 2-4. Stimulated photon echoes showing the recall efficiency of a data sequence. The dotted line represents the off resonance sequence and the solid line represents the on resonance output from the crystal. The echo efficiencies range from 80% up to 148%.

3. *Energy Sources of Echoes*

The stimulated photon echo is the basis for proposed ultra-high performance systems for memory, processing, routing and true time delay. The mechanism leading to the coherent rephasing of the medium is well understood, although there is considerable disagreement about the mechanism by which the stimulated photon echo (SPE) extracts its energy from the medium. We show by simulation and experiment that the energy of the SPE

corresponds to a drop in the population of atoms in their excited state at the time of the echo.

The stimulated photon echo is described in the literature in several different ways. First, the SPE can be modeled as a phased array of classical dipole radiators in which the spontaneous emission from the atomic population during the time of the echo radiates constructively in the direction of the echo and interferes destructively in all other directions. A second method of description is the linear scattering approach in which it is believed that the energy of the SPE arises as a linear scattering event from the spectral grating. In this approach the energy of the input pulse is redirected, due to its spectral components being attenuated and phase shifted, resulting in a SPE. In this work we show that the energy for the SPE is extracted from the atomic population and arises from a macroscopic polarization of the medium at a time τ_{21} after the third pulse.

We performed a numerical integration of the well-known Maxwell-Bloch equations for a pulse sequence of three $\pi/2$ pulses. In figure 3-1 we show the average atomic population during the time of the third pulse and the SPE for three different input pulse sequences in which τ_{21} was varied between 3.5-7 μsec. It can be clearly seen that there is a permanent drop in atomic population at the time of the SPE that is proportional to the size of the SPE. We demonstrated the drop in population experimentally by observing the fluorescence perpendicular to the direction of propagation in a Tm:YAG crystal for an input pulse sequence of three $\pi/2$ pulses. In figure 3-2 we show the fluorescence during the time in which the third pulse and SPE are propagating through the medium for three different input pulse sequences. A permanent drop in the fluorescence level occurs at the time of the SPE and clearly indicates that the echo energy comes directly from the atomic population. The experimental results are in quantitative agreement with theoretical predictions.

In conclusion we have shown theoretically and experimentally that the energy of the SPE is extracted from the atomic population. We have further shown that although they are useful modeling tools, the classical dipole array and the linear scattering filter approaches do not accurately describe the stimulated photon echo process.
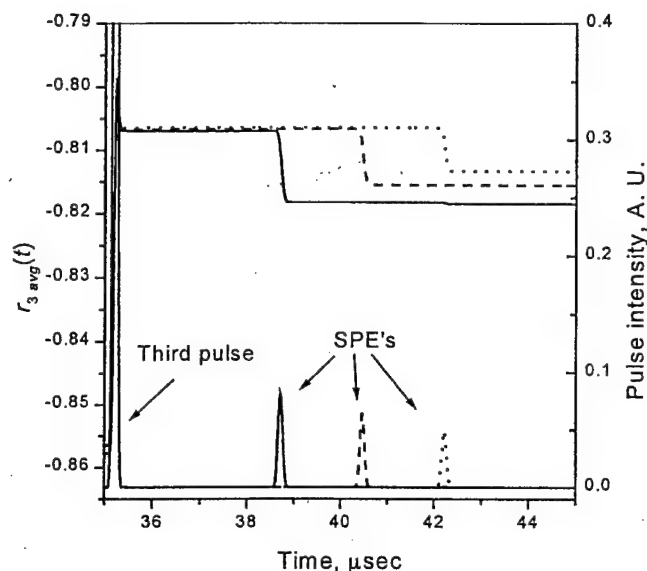
Fig 3-1. Average population (upper traces, left y-axis) for three different weighted gaussian beams with τ_{21}=3.5 µsec (solid line), 5.75 µsec (dashed line) and 7 µsec (dotted line) vs. time, along with the corresponding third pulse and SPE intensities for each case (lower traces, right y-axis).
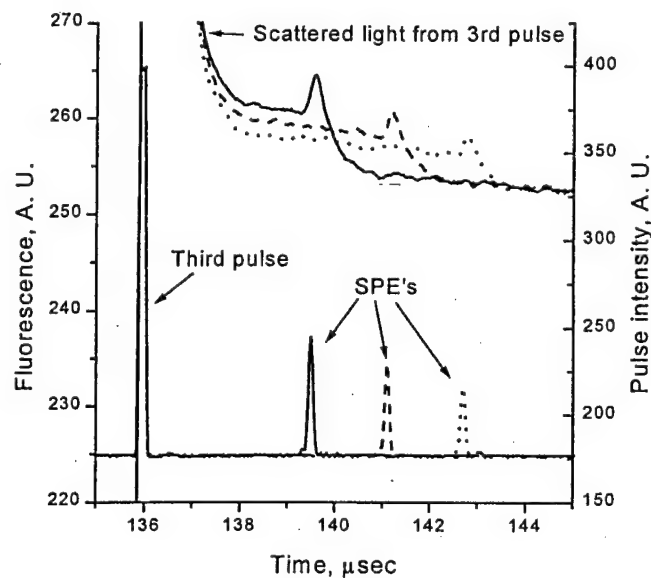

Fig 3-2. Measured fluorescence (upper traces, left y-axis) for three pulse sequences where τ_{21}=3.5 µsec (solid line), 5.75 µsec (dashed line) and 7 µsec (dotted line) vs. time. The lower traces (right y-axis) show the corresponding third pulse and SPE intensities for each case.

4. *Study on Virtual Echoes*

Time-domain four-wave mixing (TDFWM) involves coherent interaction of three temporally distinct optical waveforms in an inhomogeneously broadened transition (IBT), thereby producing a fourth distinct waveform[1-3] emitted by the medium. Two optical

14

pulses, $E_1(t)$ and $E_2(t)$ separated by a time delay τ_{21}, resonantly interfere in an IBT to write a spatial-spectral holographic (SSH) grating in its' absorption profile. If a third pulse $E_3(t)$ probes the grating at a later time t_3, then a stimulated photon echo (SPE) is emitted at $t_3 + \tau_{21}$. It has been shown that a continuous transition from a spatial grating to a spatial-spectral grating occurs when τ_{21} increases from zero[4]. Interestingly, an asymmetry in the scattered waveform occurs with this transition, where only one first-order (+) signal is emitted, and the other first-order signal (-), coined the 'virtual' echo (VE)[5], is predicted to be emitted at $t_3 - \tau_{21}$, but is not, due to causality[6].

In this project, we show that although the VE does not exist as a macroscopic polarization, there are Liouville-space coherence pathways related to the VE in a causal time domain. Relative to the SPE, these pathways are conjugate in their inhomogeneous phase evolution. By introducing a fourth input pulse $E_4(t)$ (acting to second order in dipole coupling) after the probe pulse, we experimentally demonstrate how the phase conjugate coherence pathways of the TDFWM sequence are rephased, resulting in the emission of causal signals, called here the rephased virtual echo (RVE) and the rephased stimulated photon echo (RSPE). This experimental input sequence constitutes a time-domain six-wave mixing (TDSWM) process. We experimentally demonstrate the time behavior and dephasing mechanisms of the TDSWM signals, and also perform an auto-correlation/convolution signal processing experiment to further demonstrate the phase conjugate nature of the pathways.

Time-Domain Four-Wave Mixing

Figure 3-1(a) depicts a standard stimulated photon echo experiment where two optical pulse envelopes separated by time delay τ_{21} resonantly interact with a two level ($|g\rangle$ and $|e\rangle$) IBT through dipole coupling to write a SSH grating. Each pulse has the form $E_i(t - t_i - \eta_i)\cos(\omega_0(t - \eta_i) + \phi_i)$, where the subscript $i = 1, 2$ gives the order of arrival of each waveform at time t_i in the medium at $\vec{r} = 0$, $E_i(\tau)$ is a slowly varying envelope function, ω_0 is the laser center frequency, $\eta_i = \hat{k}_i \cdot \vec{r}/c$ where $\hat{k}$ is the unit wavevector, and ϕ_i gives the phase of waveform i. The grating is described as,

$$G(\omega) \propto E_1^*(\omega)E_2(\omega)e^{i\omega(\tau_{21} - \phi_{21})} + E_1(\omega)E_2^*(\omega)e^{-i\omega(\tau_{21} - \phi_{21})}. \quad (4\text{-}1)$$

Here, $\phi_{21} = \phi_2 - \phi_1$ is the phase difference between programming waveforms and $E_i(\omega)$ is the Fourier transform of the ith applied optical envelope, $E_i(\tau_i)$. Relation (4-1) assumes all pulses propagate along a common direction.

The grating will persist for the IBT's population lifetime, T_1. If a third pulse, $E_3(t)$, probes the IBT at time t_3 within T_1, a coherent superposition (coherence) of $|g\rangle$ and $|e\rangle$ is induced that optimally rephases at $t_3 + \tau_{21}'$, creating a macroscopic polarization that causes the IBT to emit a stimulated photon echo according to

$$E_{SPE}(t) \propto \int E_1^*(\omega)E_2(\omega)E_3(\omega)\exp(i\omega(t - t_{SPE}))d\omega \quad (4\text{-}2)$$

where $t_{spe} = t_3 + \tau_{21}$. Relation(4-2) is the result of the probe interacting with the first term of relation(4-1), whereas the second (complex conjugate) term of relation (4-1) promotes a non-causal solution described as,

$$VE(t) \propto \int E_1(\omega)E_2^*(\omega)E_3(\omega)\exp(i\omega(t\text{-}t_{VE}))d\omega \qquad (4\text{-}3)$$

were $t_{VE} = t_3\text{-}\tau_{21}$. This non-causal mathematical artifact was first coined the 'virtual' echo by A.L. Bloom in a 1954 paper on nuclear spin echoes where he comments "...following the third pulse the nuclear system behaves in every way as if the virtual echo had actually occurred"[5].

As Bloom suggests, although the VE does not exist, there are coherence terms related to the VE in a causal time-domain. The next section gives a qualitative description of the induced coherence in terms of Liouville-space pathways; see reference[1] for a thorough presentation on Liouville-space non-linear optics.

Liouville-Space Pathways of Time-Domain Wave-Mixing
We assume an inhomogeneously broadened two level quantum system, with excited level e and ground level g, where in Hilbert space the density matrix

$$\rho(t) = \sum_{n,m} \rho_{nm}(t)|n\rangle\langle m| \qquad (4\text{-}4)$$

obeys the quantum Liouville equation with solution given as,

$$\rho(t) = U(t,t_0)\rho(t_0)U^\dagger(t,t_0) \qquad (4\text{-}5)$$

where the time evolution operator $U(t,t_0)$ evolves the system, between pulsed waveform interactions, by

$$U(t\text{-}t_0)|n\rangle = \exp(-\frac{i}{\hbar}H(t\text{-}t_0))|n\rangle. \qquad (4\text{-}6)$$

Here the U ($U^\dagger$) operator of equation (4-5) acting from the left (right) evolves the ket (bra) of equation(4-6).

Four-wave mixing
The Liouville-space formalism, unlike its Hilbert-space counterpart, gives information about the phase evolution of the system during population and coherence time periods in terms of pathways. A final solution is written as a sum over all pathways, constituting a path integral in Liouville-space[1]. The pathways may be realized by following the evolution of each element in the sum of equation (4-4) through the three optical interactions of the TDFWM process. Figure 4-1(c) shows the basic Liouville-space diagram to depict the pathways and figure 4-1(b) plots the corresponding inhomogeneous phase evolution for the TD4WM input sequence. Notice that figures 4-1 (a), (b) and (c) all share a common temporal axis.

In figure 4-1 (b) the phase evolution of three of the absorbers in the IBT are depicted; one at the laser center frequency, ω_0, and two at frequencies detuned as $\omega_0 + \Delta$ and $\omega_0 - \Delta$. The first element of figure 4-1(c) $|g\rangle\langle g|$ assumes the atomic population is in a ground state equilibrium previous to the application of pulse 1. Pulse 1 drives the system from its initially state into a coherence between the ground and excited states,

16

$|g\rangle\langle e|$ or $|e\rangle\langle g|$. In figure 4-1(c), an arrow with a positive slope represent the system being driven from $|g\rangle\langle g|$ to $|e\rangle\langle g|$ (dipole operator acting to first order from the left), whereas an arrow with a negative slope represent the system being driven from $|g\rangle\langle g|$ to $|g\rangle\langle e|$ (dipole operator acting to first order from the right). The density matrix is Hermetian, therefore both a positive and negative arrow takes place with each waveform interaction.

In figure 4-1(b) the spreading of the lines during $\tau_{21} = t_2 - t_1$ represents the relative dephasing, due to inhomogeneous broadening of the coherence described by equation (4-5). Dephasing occurs until pulse 2 is applied. Then the coherence is converted into a SSH grating in the excited $|e\rangle\langle e|$ and ground $|g\rangle\langle g|$ state populations, where according to equation (4-5) no phase accrues (assuming coherence loss) during the duration $\tau_{32} = t_3 - t_2$ as shown in figure 4-1(b). The grating contains information about the amplitude and phase of $E_1(t)$ and $E_2(t)$, modulated by a periodic term with period, $1/\tau_{21}$. Applying a probe pulse $E_3(t)$ to the system at t_3, stimulates two phase conjugate coherence terms from both excited and ground state population gratings as shown in figure 4-1(c). After three first-order interactions, there are eight pathways to the TD4WM process and, in general there will be 2^{N-1} pathways for a time-domain N-wave mixing sequence where each pulse acts to first order in dipole coupling.

After the probe pulse is applied the coherence phase evolution is described by equation (4-4), however the TDFWM coherence pathways of figure 4-1(c) have either the same or opposite inhomogeneous phase behavior as during the initial coherence period τ_{21} (i.e. $|e\rangle\langle g|$ is identical to $|e\rangle\langle g|$ or $|e\rangle\langle g|$ is conjugate to $|g\rangle\langle e|$). Figure 4-1(b) shows how the inhomogeneous phase evolution which occurred during τ_{21}, $\exp(-i(\omega_e - \omega_g)\tau_{21})$, is reversed, $\exp(i(\omega_e - \omega_g)(t-t_3))$, and the coherence optimally rephases at $t = t_3 + \tau_{21}$, generating a macroscopic third order non-linear optical polarization, $P^{(3)}$, culminating in the emission of the SPE. As well, there are coherence pathways that are conjugate in their inhomogeneous phase evolution and therefore have the same inhomogeneous phase behavior during τ_{21} as they did during τ_{32}; these pathways continue their dephasing at t_3. Figure 4-1(b) shows how the virtual echo is realized if time is allowed to run in reverse (dashed lines) after the application of the probe pulse. The system appears to undergo a non-causal rephasing event at $t_{VE} = t_3 - \tau_{21}$.

Six-wave mixing to rephase the virtual echo

Similar to a traditional two-pulse photon echo experiment, a fourth pulse, which acts to second order in dipole coupling, can reverse the inhomogeneous phase evolution of an induced coherence. Figure 4-2(a) shows the TDSWM input sequence, where $E_4(t)$ is introduced into the IBA after $E_3(t)$. Figure 4-2(b) depicts how the TDFWM coherence pathways undergo rephasing ($|e\rangle\langle g| \rightarrow |g\rangle\langle e|$ and $|g\rangle\langle e| \rightarrow |e\rangle\langle g|$) and contribute to transient TDSWM signals, called the re-phased stimulated photon echo (RSPE) and rephased virtual echo (RVE).

17

Included in figure 4-2 are all of the significant outputs that pulse 4 contributes, including two additional TDFWM signals: a SPE from the pulse 1, 2, 4 sequence where pulse 4 is acting to first order and a two-pulse photon echo ($2PE_{34}$) from pulses 3 and 4 where pulse 4 is acting to second order. It may be more intuitive to view this TDSWM process as performing a 2PE experiment in a medium with a periodic spectral grating pre-programmed into it. As shown in figure 4-2(a), the RVE and RSPE are then viewed as time-domain sidebands of the $2PE_{34}$, where their timing about the $2PE_{34}$ ($t_{TDSWM} = t_{2PE_{34}} \pm \tau_{21}$), indicates the period of the pre-programmed grating.

Experiments

The experiments were performed on the $^3H_4$-$^3H_6$ transition of $Tm^{3+:}$ YAG (0.1 at. %) maintained at 4.2 K in a continuous flow liquid He vapor cryostat. The 793nm cw-output of a Ti-Sapphire ring laser was resonant with this transition and crafted into optical pulses by an acousto-optic modulator driven by an arbitrary waveform generator. The pulses were incident upon the sample in a collinear input geometry. In all experiments, the input pulse areas were determined through the optical nutation technique of reference[7] and set to $\pi/2$ for pulses 1, 2, 3 and π for pulse 4. The output signals were detected on a silicon photodiode and events were captured on a 500 MHz digitizing oscilloscope. It should be noted that although $Tm^{3+:}$ YAG acts as a three level bottle-necked system under 793nm excitation, by making $\tau_{31} = 1\, ms$ the decay dynamics are reduced to a two-level system in the $^3H_4$-$^3H_6$ transition and the above analysis is valid

Demonstration of time-domain six-wave mixing with brief pulses

We first demonstrate rephasing of the virtual echo by using the experimental architecture of figure 4-2a where all four input pulses are brief (240 ns). Figure 4-3 shows a single shot capture of TDSWM with $\tau_{21} = 1.45\mu s$, $\tau_{31} \sim 1\, ms$ and $\tau_{43} = 9.42\mu s$. The trace shows all expected four and six wave mixing outputs with the RVE and RSPE having temporal locations consistent with the rephasing of the four-wave mixing Liouville-space pathways. Included are arrows that indicate the direction in time that the signals will move when τ_{21} is increased, keeping τ_{31} and τ_{43} fixed.

By varying τ_{21}, the homogeneous dephasing time of the medium T_2 can be obtained through intensity decay measurements of the echoes, predicted as,

$$I = I_0 \, \exp(-2\tau_{coh} / T_2), \qquad (4\text{-}7)$$

where τ_{coh} denotes the time duration that the atoms spend in a coherent superposition leading up to the echo event. In particular, for the present four and six-wave mixing signals of interest,

$$\text{SPE: } \tau_{coh} = 2\tau_{21} \qquad (4\text{-}8)$$

$$\text{SPE}_{124} : \tau_{coh} = 2\tau_{21} \qquad (4\text{-}9)$$

$$\text{RSPE: } \tau_{coh} = 2\tau_{43} \qquad (4\text{-}10)$$

$$\text{RVE: } \tau_{coh} = 2\tau_{43} - 2\tau_{21} . \qquad (4\text{-}11)$$

Equations (4-10) and (4-11), based on the Liouville-space pathway description of the TDSWM coherence, predicts that the RSPE is not expected to decay with increased τ_{21}, whereas all other signals will decay according to equation (4-6), including the RVE. It

should be noted that although an increase in τ_{21} will effect the temporal location of the RSPE, as depicted in figure 4-3, its amplitude should remain unchanged; for every unit of time that τ_{21} is increased, the RSPE moves closer to pulse 4 by the same increment, thereby keeping the overall coherence time constant.

Figure 4-4 plots averaged (x16) peak powers of the SPE, SPE_{124}, RSPE and RVE versus τ_{21}, along with first order exponential decay fits for the SPE, SPE_{124}, RVE and a linear fit for the RSPE. For this data, all inputs were brief 120ns pulses and τ_{21} was varied from .6144 µs to 7.9872 µs in .2048 µs increments, keeping fixed $\tau_{31} \sim 1\ ms$ and $\tau_{43} = 4.71 \mu s$. The RVE first order exponential decay fit gives a value of $T_2 = 24.94$ µs, in close agreement with $T_2 = 24.08$ µs obtained from the SPE decay. The RSPE exhibits a very small linear decay of slope 2.18E-5, which is not predicted by our simple model. We attribute this to a long term drift of the laser's power and population decay of the grating. The break in the data near $\tau_{21} \sim 4.7 \mu s$ occurs because SPE_{124} and PE_{34} interfere, making their peaks indistinguishable. From this point, as τ_{21} becomes larger than τ_{43}, pulse 4 acts on the coherence such that the SPE and RSPE are no longer emitted.

Optical signal processing

It has been shown that if $E_1(t)$ is a brief reference pulse and $E_2(t)$, $E_3(t)$ are identical temporally modulated waveforms (TMW's), then the temporal envelopes described by relations (4-2) and (4-3) closely approximate the auto-convolution and auto-correlation functions, respectively[8]. Under such conditions, relations (4-2) and (4-3) may be rewritten in the time-domain as,

$$E_{SPE}(t) \propto E_2(t) * E_2(t\text{-}t_{SPE}) \tag{4-12}$$

and

$$VE(t) \propto E_2(t) \otimes E_2(t\text{-}t_{VE}), \tag{4-13}$$

where the symbols $\otimes$ and $*$ represent auto-correlation and auto-convolution operations respectively.

We demonstrate TDSWM using the 5-bit bi-phase Barker code - a phase-modulated returns to zero sequence of 5 brief pulses {1,1,1, -1,1} - as the TMW for $E_2(t)$ and $E_3(t)$, while keeping $E_1(t)$ and $E_4(t)$ brief reference pulses. Figure 4-5(a) shows the inputs and expected outputs for this experimental input sequence. The temporal shape of the RSPE and RVE are predicted to be auto-convolution and auto-correlation of the Barker code, respectively. Here, for simplicity, we ignore the SPE_{124} and PE_{34} that pulse four contributes.

Figure 4-5(b) shows an experimental demonstration of the input scheme depicted in figure 4-5(a) where each input pulse is 150 ns in duration, $\tau_{21} = 1.843 \mu s$ and $\tau_{34} = 5.734 \mu s$. The RVE and RSPE clearly have the temporal shape and location consistent with the rephasing of relations (4-12) and (4-13), verifying that the RVE and RSPE are causally related to the phase conjugate Liouville coherence pathways of TD4WM. As expected, figure 4-5(b) also contains the SPE_{124} and PE_{34}, which represent the barker code and its time-reversed replica. Deviations from the expected theoretical

output can be attributed to higher order non-linear interactions that can be expected to occur with such complex input schemes.

In conclusion, we've shown that the scattering symmetry that is lost in the electric field, when a transition from a spatial grating to a spatial-spectral grating occurs, is retained in the Liouville pathways of the induced coherence by experimentally rephasing the VE and SPE. We performed coherence decay and optical signal processing time-domain six-wave mixing experiments to verify the phase conjugate relationship between the Liouville-space coherence pathways associated with the VE and SPE.

References for section 4

[1] S. Mukamel, *Principles of Nonlinear Optical Spectroscopy*, Oxford Univ. Press. (1995).

[2] A. Rebane, and R. Kaarli, Chem. Phys. Lett. **101**, 317 (1983).

[3] T. W. Mossberg, Opt. Lett. **7**, 77 (1982).

[4] Duppen and D. A. Wieserma, J. Opt. Soc. Am. B. **3**, 614 (1986).

[5] Arnold L. Bloom, Phys. Rev. **98**, 1105 (1955).

[6] A. Rebane, S. Bernet, A. Renn and U. P. Wild. Opt. Comm. **86**, 7 (1991).

[7] Y. Sun, G. M. Wang, R. L. Cone, R. W. Equall, M. J. M. Leask, Phys. Rev. B **62**, 15443 (2000).

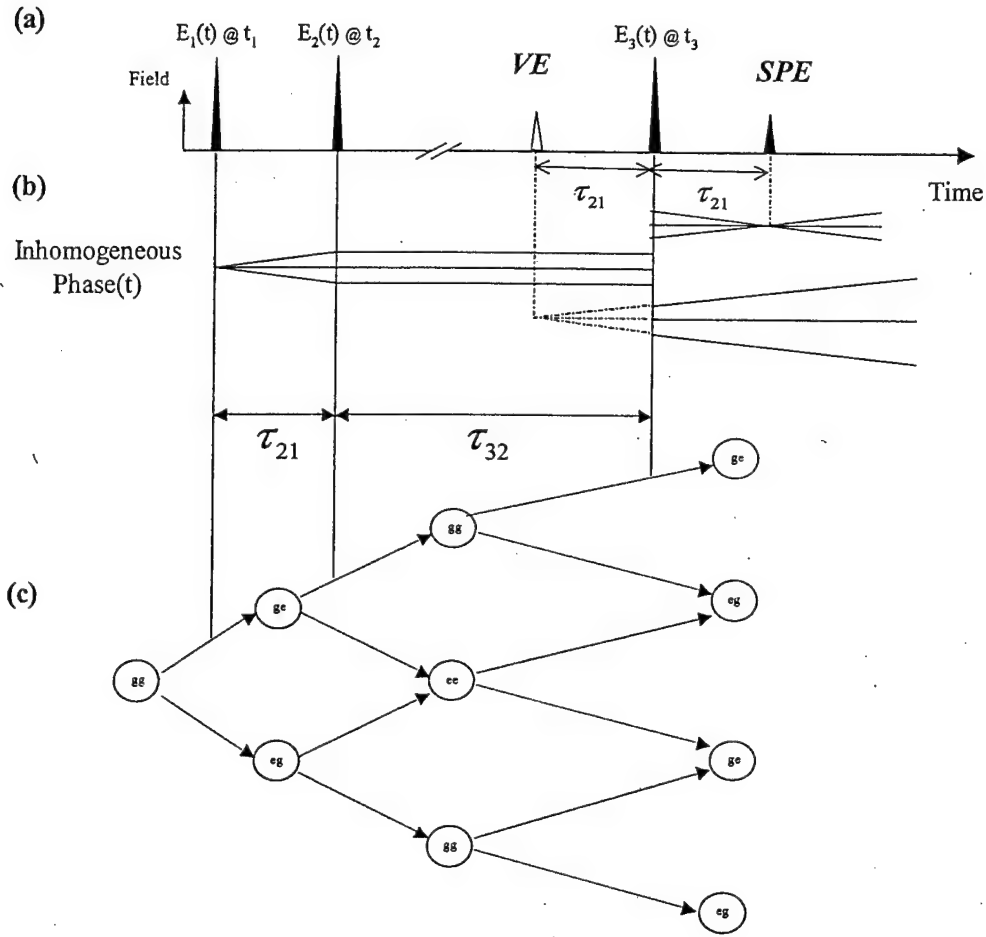[8] Y. S. Bai, W. R. Babbitt, N. W. Carlson, and T. W. Mossberg, Appl. Phys. Lett. **45**, 714 (1984).

Fig. 4-1: A traditional stimulated photon echo input scheme (a), inhomogeneous phase evolution paths for the time-domain four wave mixing process (b) and the basic Liouville-space diagram for describing the pathways in a perturbative description of time domain four wave mixing in a two-level system, with ground $|g\rangle$ and excited $|e\rangle$ states (c). After pulse 3, the two pathways of the inhomogeneous phase diagram (b) are given arbitrary vertical offsets in order to distinguish them.

21

(a)

$E_4(t)$

$E_1(t)$ $E_2(t)$ $E_3(t)$

Field

VE   SPE SPE_{124} RSPE PE_{34} RVE

Time

τ_{21} τ_{32} τ_{43} τ_{21} τ_{21}

(b)

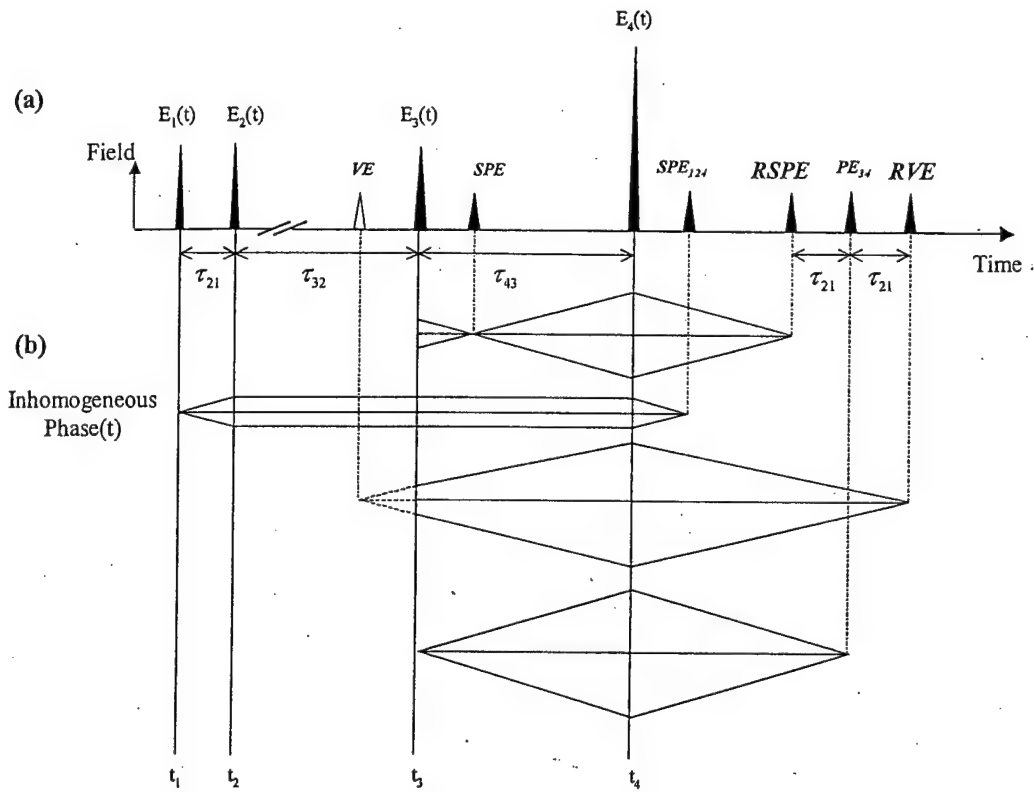Inhomogeneous
Phase(t)

t_1 t_2 t_3 t_4

Fig. 4-2: Pulse 4 is introduced at t_4 into the four-wave mixing sequence of figure 4-1 (a). This reverses the inhomogeneous phase evolution of the induced TDFWM coherence pathways, promoting time-ordered echo events to be emitted by the medium, called the rephased stimulated photon echo (RSPE) and rephased virtual echo (RVE) (b). Pulse 4 also contributes a two-pulse photon echo (PE_{34}) and a stimulated photon echo (SPE_{124}). The RSPE and RVE are predicted to occur at τ_{21} about PE_{34}.
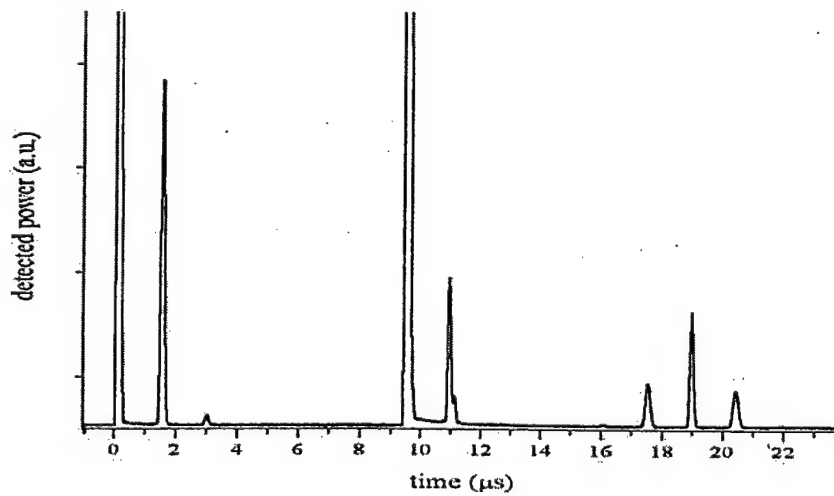

Fig. 4-3: Experimental demonstration of the TDSWM input sequence depicted in figure 2(a), using brief pulse (240 ns) inputs.
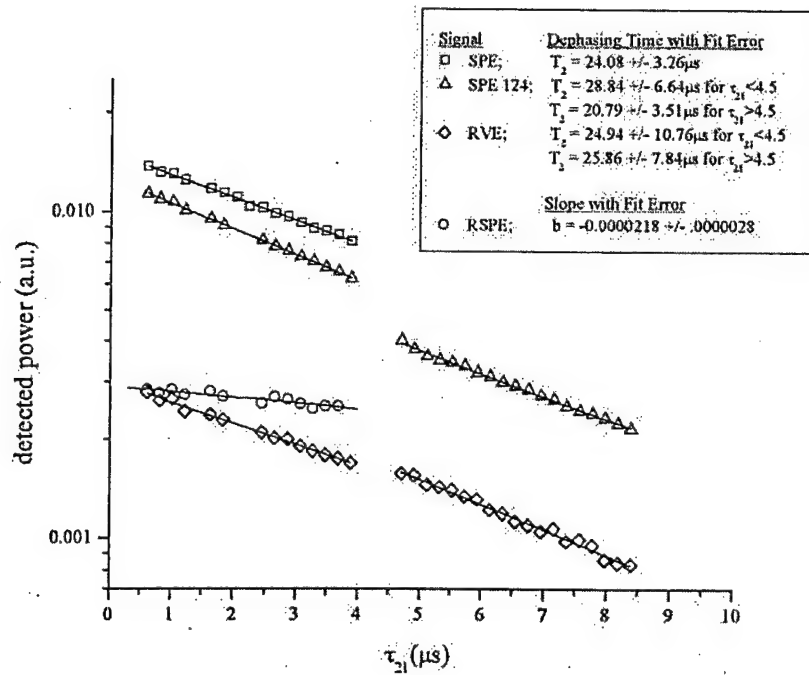
Fig. 4-4: Detected power of the SPE, SPE$_{124}$, RSPE and RVE vs. programmed time delay τ_{21} and corresponding exponential decay and linear fits.
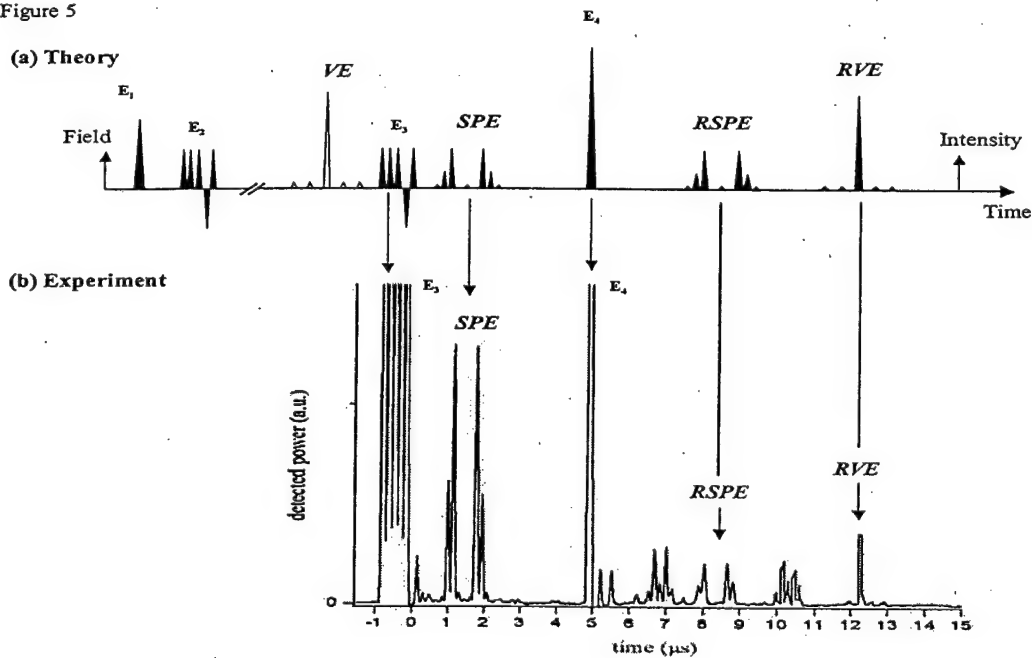
Figure 5

Fig. 4-5: The TDSWM input sequence using the 5-bit barker code for $E_2(t)$ and $E_3(t)$, where the temporal shape of the SPE and RSPE is predicted to be an auto-convolution of the barker code and the shape of the VE and RVE is predicted to be an auto-correlation (a). (b)Experimental demonstration of the input and output sequence of (a).

23

5. *BPSK and QPSK correlation*

Spatial-spectral holographic (SSH) devices combine spectral hole burning (SHB) with conventional holography to perform real time memory and signal processing functions, in particular, correlations with signals of arbitrary modulation. SSH devices can operate at bandwidths greater than 10 GHz, have time-bandwidth products in excess of 10^5 and can potentially enhance optical communications capabilities.[1,2,3] Correlators have general applicability in many signal processing and memory implementations such as pattern recognition, database searching, associative memories, data packet address header decoding, and spread spectrum communications. SSH devices are ideally suited to perform correlations with multi-phase encoded information, such as binary and quadrature phase-shift key (BPSK and QPSK) modulation. We have shown that eight different erbium-doped insulating crystals have the required frequency-selective and coherence properties to provide SSH devices at more than eight operating wavelengths in and near the important 1.5 μm communication window.[3,4]

There have been numerous demonstrations of SSH correlators at wavelengths other than 1.5 μm, including header-decoder demonstrations at 580 and 793 nm.[5,6] Our previous demonstration[7] of an SSH header-decoder was the first time-domain SSH correlations performed at 1.5 μm. In this work we demonstrate our use of the $Er^{3+}:Y_2SiO_5$ (Er:YSO) SHB material to obtain excellent signal fidelity by optimizing the optical pulse areas in a 1.5 μm SSH optical correlator using BPSK and QPSK codes, 30 symbols in length. We believe this to be the maximum number of symbols yet achieved for SSH correlations. As well, we believe these are the only SSH based correlations using QPSK codes.

The phase-shift keyed (PSK) codes[8] used in this work were developed for Direct Sequence/Spread Spectrum (DS/SS) Communications.[9,10] DS/SS is employed for non-centralized, multiple access, coherent optical communication with an added degree of security. DS/SS implementations rely on the correlation properties of coded spread spectrum signals. In Rf links these typically take the form of BPSK modulation. Correlating codes with a phase alphabet of greater than two characters in real time, at multi-GHz rates, is not possible electronically.

The correlation is performed in two stages. First, the SHB medium is programmed with an SSH grating by the application of a programming pulse pair, shown in figure 5-1. The first of these pulses contains the temporal pattern that the correlator is programmed to recognize and can be a signal with any arbitrary combination of amplitude, frequency and phase modulation. The second pulse is a brief reference pulse, spectrally flat over the bandwidth of the temporal pattern. The pattern and reference pulses, with combined duration less than the SHB material phase memory lifetime, interfere to form a spatial-spectral population grating in the inhomogeneously broadened absorption line in Er:YSO. This grating contains the spectral product of the Fourier components of the two programming pulses and is stored for the duration of the upper state lifetime. In the second stage, the stored grating can process another arbitrarily patterned pulse. The stimulated photon echo's temporal structure is the square of the cross-correlation of pulses one and three convolved with the reference pulse.[11] Because the correlation process takes place entirely within the SHB medium, an SSH correlator can be quite simple requiring only the crystal, optics, cryogenics and a modest magnetic field for Er^{3+} materials. In this demonstration, we programmed the crystal to recognize patterned pulses

24

that were PSK modulated and were previously selected by Very Fast Simulated Re-annealing using the criteria of minimizing the aperiodic auto- and cross-correlation sidelobes.[8] In eight separate experiments we used four distinct codes, two BPSK and two QPSK. The coded programming pulse was applied to the crystal prior to a brief reference pulse. Application of another coded pulse produced correlation echoes, which were either auto-correlations or cross-correlations depending on whether a replica of the programmed code or an orthogonal code from the same PSK family was applied, respectively.

The correlator consists of a 0.001% Er:YSO crystal mounted between button sized NdFeB permanent magnets, providing a magnetic field of $H_o = $ ~2.5 kG. The crystal and magnets resided in a 1.5 K cryostat. Under these conditions, the coherence lifetime was ~70 μs and the upper state lifetime was ~10 ms. Additional apparatus, used to examine correlator fidelity, included an external cavity diode laser, coupled into an erbium doped fiber amplifier. These were utilized in combination with an acousto-optic modulator (AOM) to produce coded and brief pulses for the programming and processing stages. These pulses imitated the pulses that might be used in a real device. The AOM diffracted output beam was focused to a beam waist radius of $w_0 = 100$ μm in the crystal and had nominal peak power of 8 mW. An arbitrary waveform generator (AWG) synthesized the electrical AOM drive pulses and controlled their phases and relative amplitudes. The AWG was programmed to produce the 3 μs total duration (100 ns/symbol) coded pulses. The BPSK code pair was A(011000110100011101001001001111) and B(010001000000011100101011110000). The QPSK code pair was A(000012001023132111031301303230) and B(223223012103332010020021233023). Here each number, m, in parentheses, represents a symbol from the M-PSK (M=2 is BPSK and M=4 is QPSK) phase alphabet $A_M = \{\exp(i2\pi m/M), m = 0, ..., M-1\}$ and corresponds to the phase shift imparted to the carrier by the AWG. A brief reference pulse of 100 ns duration, with no phase coding, followed each coded pulse by 6 μs. The programming and processing stages were separated by 100 μs. Correlation echoes were detected on an InGaAs photodiode whose minimum detectable power (0 dB SNR) was ~250 nW. The photodiode output was fed into a digitizing oscilloscope for single-shot signal capture.

Frequency jitter of the laser profoundly influences the single shot fidelity and shot to shot reproducibility of our experiments. Spectral analysis of the beat note between two lasers of this type indicates that the spectral width of the laser jitter envelope on a 50 ms time scale is ~1 MHz. This spectral width is large compared to the inverse of the coded pulse duration and can therefore cause the spectrum of the third pulse to mismatch the stored grating resulting in severe echo distortion. We observe this effect in our modeling as well.

Laser jitter presents an obstacle to examining other fidelity diminishing effects such as coherent saturation, and excitation pulse and echo propagation. We overcame this obstacle by selecting single-shot echoes for averaging. For auto-correlations we chose to discriminate single shots on the basis of central lobe intensity. This technique was not useful for the cross-correlation echo experiments, as the side-lobes, which constitute the entire signal, were within the noise floor of our photo-detector. To overcome this problem we performed a separate simultaneous stimulated echo experiment in a different part of the crystal. The pulses for this separate echo experiment were produced by a second AOM optically in series with the first AOM and timed to sample the same laser

25

light as the correlator pulses. The size of the echo obtained was used to select single shots whose fidelity was not influenced significantly by laser jitter.

Numerical simulations of the optical Bloch equation were performed to model the interaction of the phase encoded and brief pulses with the holeburning medium. Our simulations neglect the non-uniform spatial intensity profile of the optical beam in the crystal. Effects on echo fidelity resulting from a spatially dependent spectrum of Rabi frequencies in the crystal are therefore not modeled. The coherence decay of the medium was treated as an instantaneous event, occurring between pulses two and three, and ignored otherwise. This model is valid provided the temporal duration of the programming pulses is small compared to the coherence lifetime. The simulator was used to model experimental auto- and cross-correlations for both the BPSK and QPSK code pairs using the same approximate pulse areas. It was also used to model the effects of coherent saturation distortion on the auto- and cross-correlations for the BPSK auto- and cross-correlations and to model the effects of laser jitter on the echo signal.

Experiment and simulation results are presented in figures. 5-2 and 5-3. The experimental traces are the average of 100 selected single shots with the photodetector background subtracted. The signal averaging resolved the correlation echo sidelobes from the photodetector noise floor and allowed signal fidelity examination. All correlations, experimental and simulated, have been normalized to the average auto-correlation central lobe of that PSK family. It can be seen that the experimentally obtained correlation echoes are in excellent quantitative agreement with the simulated signals. figure 5-1 shows that auto-correlations exhibit sharp contrast between their central lobe and side-lobes making them suitable for threshold detection. The cross correlations exhibit low intensity at the expected auto-correlation-central-lobe arrival time, making them well suited for synchronous threshold detection.

Fractional side-lobe levels (FSL) are a metric used to evaluate the relative performance of a set of codes. The FSL is defined, for the mathematically ideal discrete auto- and cross-correlation functions (ACF and CCF), as the ratio of the maximum correlation function side-lobe to the length of the code and is usually given in dB as $20 \times \log_{10}(\text{FSL})$. The ACF and CCF are calculated from the definitions found in Ref. 10, Chapter 8. For the BPSK codes the FSL for both the ACF and CCF is −13.979 dB. For the QPSK codes the ACF-FSL is −16.532 dB and the CCF-FSL is −13.860 dB. By contrast, the FSL's for the experimental and simulated (E-FSL and S-FSL) correlations are calculated by taking the ratio of the integrated intensities of the maximum correlation side-lobe and the auto-correlation central lobe. The E-FSL and S-FSL values for each auto- and cross-correlation accompany the data in figures. 5-2 and 5-3. The slight mismatch between the correlation function FSL values and those obtained through simulation and experiment is in part owing to the difference in the definition of the two quantities and the fact that the mathematically ideal FSLs are obtained assuming an ideal, experimentally unrealizable, delta function reference pulse. The sidelobes in all the experimental correlations exhibit some mismatch with the simulation. Simulations suggest that the pulse areas used (0.04π/symbol) are sufficiently large to cause minor coherent saturation of the holeburning medium. This, combined with the difficulties involved in estimating experimental pulse areas, causing the simulations to use only approximately the same pulse areas has contributed to this mismatch. Furthermore, the experiment excitation pulses suffered distortions due to modulator bandwidth limitations,

this led to some distortion of the correlations. We have begun to investigate the mechanisms that degrade signal fidelity in an SSH correlator and are currently pursuing a correlator whose performance will not be limited by modulator bandwidth and laser stability.

In summary, we have demonstrated excellent signal fidelity in an SSH correlator using the Er:YSO SHB medium which provides an operating wavelength in the important 1.5 μm communications band. These correlations were performed using, as a model system, 30 symbol BPSK and QPSK codes optimized for DS/SS communications. We believe this is the first demonstration of correlations by this time-domain technique with such optimized codes of greater than 20 symbols in length, and the first SSH based correlations with QPSK codes.

References for section 5

[1] T. W. Mossberg, *Opt. Lett.* **7,** 77 (1982); W. R. Babbitt and T. W. Mossberg, *Appl. Opt.* **25**, 962 (1986).
  A. Rebane, R. Kaarli, P. Saari, A. Anijdg, and K. Timpmann, *Opt. Commun.* **47**, 173 (1983); P. Saari, R. Kaarli, and A. Rebane, *J. Opt. Soc, Am. B* **3**, 527 (1986).

[2] Y. Sun, T. L. Harris, R. L. Cone, to be published.

[3] R. M. Macfarlane, T. L. Harris, Y. Sun, R. L. Cone, and R. W. Equall, *Opt. Lett.* **22**, 871 (1997).

[4] X. A. Shen and R. Kachru, *Opt. Lett.* **20**, 2508 (1995).

[5] T. Wang, H. Lin, and T. W. Mossberg, *Opt. Lett.* **20**, 2541 (1995).

[6] T. L. Harris, Y. Sun, R. L. Cone, R. M. Macfarlane, and R. W. Equall, *Opt. Lett.* **23**, 636 (1998).

[7] W. R. Babbitt, A. Mohan, and J. A. Ritcey, Proc. SPIE, 3228, 354-365, Multimedia Networks, 4-5 November 1997, Dallas, TX.

[8] J. Proakis, *Digital Communications*, Wiley-Interscience, (1995).

[9] J. D. Gibson, ed., *The Communications Handbook*, CRC Press Inc., (1997).

[10] Y. S. Bai, W. R. Babbitt, N. W. Carlson, and T. W. Mossberg, *Appl. Phys. Lett.* **45**, 714-716 (1984).
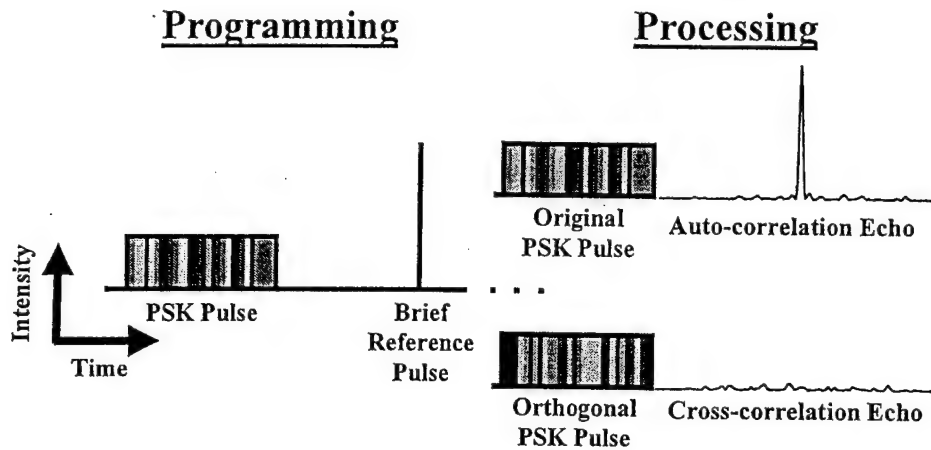
Fig. 5-1. Representation of correlator pulse sequences. Four state gray scale within the patterned pulses represents QPSK alphabet. Programming stage: patterned pulse, PSK encoded, interferes with reference pulse to form SSH grating. Processing stage: either the same PSK pulse as programmed or an orthogonal one is processed creating an auto- or cross-correlation echo, respectively. Correlation echoes are actual experimental data.
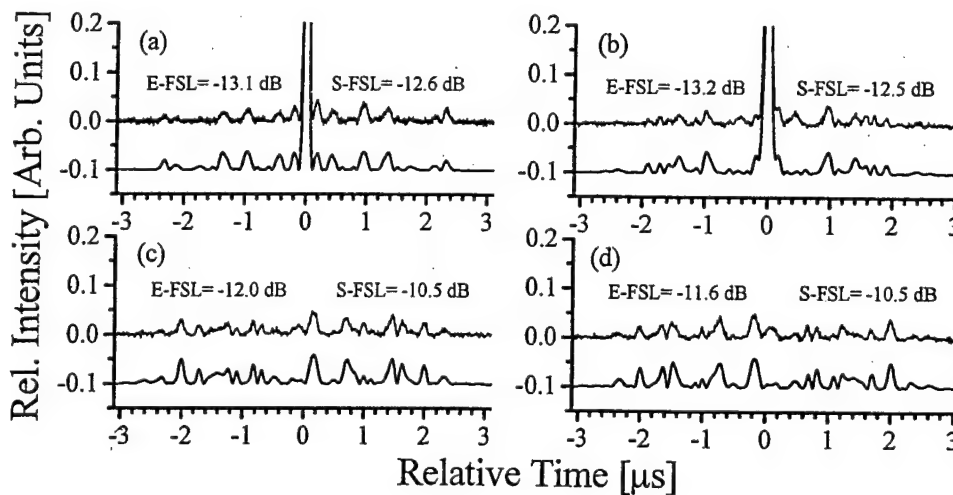

Fig. 5-2. BPSK correlation results. Top and bottom traces in each graph are experiment and simulation, respectively. A negative offset has been added to the simulation in all cases for clarity and auto-correlations have been truncated for side-lobe comparison. (a) & (b) Auto-correlations for BPSK codes A and B, respectively. (c) & (d) Cross-correlations between BPSK codes. (c) is for the case where code A is programmed and code B is processed. (d) is the opposite scenario. The Experiment and Simulation Fractional Side-lobe Levels (E-FSL and S-FSL) are the ratio of the side-lobe and auto-correlation central lobe integrated intensities.
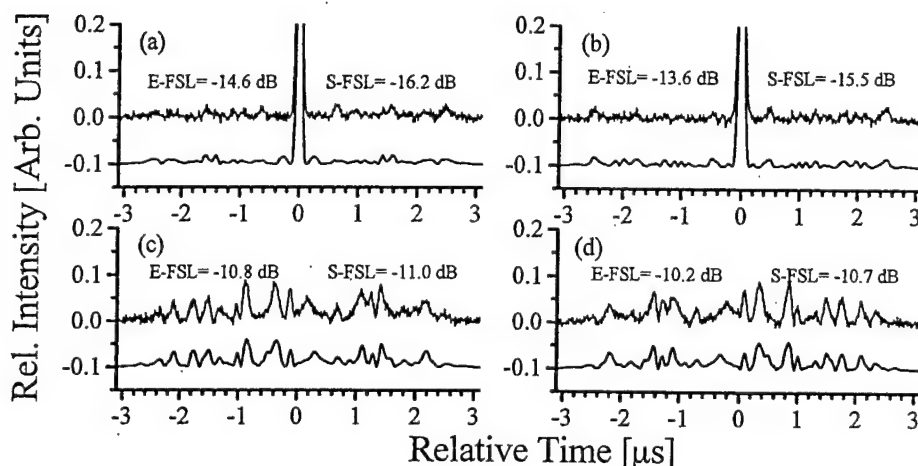
Fig. 5-3. QPSK correlation results: (a) and (b) are for auto-correlations; (c) and (d) are for cross-correlations, as in Fig. 2.

6. *Nutational Echoes*

The investigation was initiated by the requirement of understanding the continuous processing and efficient reading. Nutational behavior of echoes happens when the echoes are temporally longer than the delay and the Rabi oscillation period. Under these conditions, the echoes also propagate in both causal and non-causal directions. These are new discoveries in the field and significant to understanding the physics of the optical coherent transients. The investigation resulted in two publications in peer review journals and two conference talks.

Stimulated photon echo processes in inhomogeneously broadened absorptive media have been considered possible tools for the realization of optical memory and optical processing devices with high bit rates and large time bandwidth product[1,2]. The basic procedure involves two programming pulses that record their amplitude and phase information as a spatial-spectral hologram. This is done by exciting the inhomogeneously broadened absorbers from the ground state to the excited state. Next a third pulse probes the medium, which generates a time-delayed output optical field, which contains information about the input programming and probe pulses. Some of the applications, such as optical coherent transient true-time delay and optical analog correlation[3,4], require the third pulse (the probe) to be temporally long or even continuous. This requirement results in two major differences from the situation with a brief probe. First, an angled beam configuration has to be employed, instead of a collinear one, to spatially distinguish the output echoes from the inputs since the transmitted inputs are temporally overlapped with the echoes. Second, material saturation effects must be considered. Although the long probe pulse can be amplitude or phase modulated to reduce the saturation at some frequencies the output echo still suffers from the saturation effects when the probe time eventually exceeds certain limit at a given optical power. To study the echo's temporal behavior with a long probe field, a stimulated photon echo (SPE) process with two brief programming pulses followed by a constant quasi-continuous probe pulse is a simple case to begin with. As is well known, an electric field with an amplitude of a step-function interacting with an

inhomogeneously broadened two-level atomic system gives rise to an oscillatory behavior of the transmitted field and is referred to as optical nutation[5]. The optical nutation signal has been used as an efficient spectroscopic measurement tool to study gaseous atomic and molecular system, as well as rare-earth ion doped crystals.[6,7] However, less attention has been paid to the interaction of a long probe with the medium that has a spatial-spectral grating programmed in it.

In our investigation we have focused on the coherent saturation effects of the SPE from a long probe by studying the optical nutation signals and the spatial and temporal behavior of the echoes generated by two brief programming pulses and a long probe pulse with a duration comparable to the medium's coherent dephasing time, T_2. In the following sections presenting the results, we will start with a theoretical analysis using Maxwell-Bloch equations with an angled beam configuration in section a. The analytic field solutions for optically thin medium will be derived for the quasi-continuous probe fields along each of the two propagating directions. The experiments in Tm^{3+}:YAG crystal will be described in section b. The nutational behavior of the stimulated photon echoes was observed at different delays with various probe powers. The echoes stimulated by the long probes were also observed propagating in both directions, which is completely different from the brief pulse echo exiting in only one direction. The experimental results will be discussed in section c along with the numerical simulations from a newly developed Maxwell-Bloch simulator. This simulator considers the beams as having a spatial Gaussian mode in and optically thick medium and the experimental results are consistent with the simulations.

Theoretical Analysis with Bloch-Maxwell Equations

A theoretical modeling of OCT processes with an angled beam configuration has been recently developed based on Maxwell-Bloch equations.[8] The schematic of the approach is illustrated in figure 6-1. In a thin layer of medium, dz, located at z, the fields are
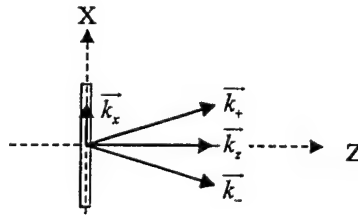

Fig. 6-1 The angled beam configuration for a stimulated photon echo process. All input and output fields are only allowed to propagate along either $\overrightarrow{k_+} = \overrightarrow{k_z} + \overrightarrow{k_x}$ or $\overrightarrow{k_-} = \overrightarrow{k_z} - \overrightarrow{k_x}$ by the phase matching condition.

assumed plane wave propagating along two directions, $\overrightarrow{k_+} = \overrightarrow{k_z} + \overrightarrow{k_x}$ and $\overrightarrow{k_-} = \overrightarrow{k_z} - \overrightarrow{k_x}$, where $\left|\overrightarrow{k_z}\right| \gg \left|\overrightarrow{k_x}\right|$. The state of the atoms driven by the combined field of $\Omega^+(z,t)$ along $\overrightarrow{k_+}$ and $\Omega^-(z,t)$ along $\overrightarrow{k_-}$ can be described by the Bloch vectors as the atomic population inversion, r_3, and the two atomic polarization components, in phase and in quadrature with the field, r_1 and r_2, respectively. The Bloch equations are modified as,

$$\frac{dr_1(x,z,t,\Delta)}{dt}=\Delta r_2(x,z,t,\Delta)+r_3(x,z,t,\Delta)\Omega_S(x,z,t)-\frac{r_1(x,z,t,\Delta)}{T_2} \tag{6-1}$$

$$\frac{dr_2(x,z,t,\Delta)}{dt}=-\Delta r_1(x,z,t,\Delta)+r_3(x,z,t,\Delta)\Omega_C(x,z,t)-\frac{r_2(x,z,t,\Delta)}{T_2} \tag{6-2}$$

$$\frac{dr_3(x,z,t,\Delta)}{dt}=-r_2(x,z,t,\Delta)\Omega_C(x,z,t)+r_1(x,z,t,\Delta)\Omega_S(x,z,t)-\frac{r_3(x,z,t,\Delta)-1}{T_3} \tag{6-3}$$

where the field components,

$$\Omega_C(x,z,t)=\Omega^+(z,t)\cos(k_x x)+\Omega^-(z,t)\cos(k_x x)$$

$$\Omega_S(x,z,t)=-\Omega^+(z,t)\sin(k_x x)+\Omega^-(z,t)\sin(k_x x),$$

and Δ denotes the frequency detuning of the atomic resonance from the driving frequency, T_2 is the coherent dephasing time and T_3, the population decay time. The propagation effects of the fields through the medium can be derived from the Maxwell equations as

$$\frac{d\Omega^+(z,t)}{dz}=\frac{\alpha}{4\pi^2}\int_0^{2\pi}\int_{-\infty}^{\infty}\left[r_2(x,z,t,\Delta)\cos(k_x x)+r_1(x,z,t,\Delta)\sin(k_x x)\right]g(\Delta)d\Delta\,d(k_x x) \tag{6-4}$$

$$\frac{d\Omega^-(z,t)}{dz}=\frac{\alpha}{4\pi^2}\int_0^{2\pi}\int_{-\infty}^{\infty}\left[r_2(x,z,t,\Delta)\cos(k_x x)-r_1(x,z,t,\Delta)\sin(k_x x)\right]g(\Delta)d\Delta\,d(k_x x). \tag{6-5}$$

Here the variables z and t are decoupled in a retarded time frame by assuming the wave travels forward along the z-axis without any back reflection, $g(\Delta)$ represents the inhomogeneous line shape. Numerical solutions of equations (6-1) through (6-5) are usually required to study angled beam OCT processes involving arbitrary input fields, including the SPE from a continuous probe. Simulations will be discussed in section 4 along with the experimental results.

With the equations shown above, the temporal shape and the propagation of a continuous field induced SPE can be predicted with analytical solutions for a simplified case. This case considers the interaction between a continuous input field and a medium with an initial spatial-spectral grating distribution of the atomic population. We make the assumptions as following.

1) The medium starts from a previously programmed initial state at time, $t = 0$, as,

$$\begin{pmatrix} r_{10}(\Delta) \\ r_{20}(\Delta) \\ r_{30}(\Delta) \end{pmatrix}=\begin{pmatrix} 0 \\ 0 \\ w_0+g_0\cos(\Delta\tau_d+2k_x x) \end{pmatrix},$$

which can be created by two programming pulses incident along $\overrightarrow{k_+}$ and $\overrightarrow{k_-}$, respectively, the second pulse temporally delayed by τ_d with respect to the first one.

2) The constant probe field corresponds to a constant input Rabi, Ω_0, provided the atoms have a single dipole moment.

3) The medium is optically thin ($\alpha L \ll 1$), $g(\Delta) = 1$ over the detuning range of interest, and the population decay can be ignored for time scales comparable to T_2 since $T_2 \ll T_3$.

Under these conditions, equations (6-1) to (6-3) can be solved for a probe incident along $\overrightarrow{k_+}$ as,

$$r_1(x,t,\Delta) = e^{-t/T_2}r_{30}(\Delta)\{\Delta\Omega_0\cos(k_x x)[1-\cos(\sqrt{\Omega_0^2+\Delta^2}t)]/(\Omega_0^2+\Delta^2)$$
$$+\Omega_0\sin(k_x x)\sin(\sqrt{\Omega_0^2+\Delta^2}t)/\sqrt{\Omega_0^2+\Delta^2}\}$$
$$r_2(x,t,\Delta) = e^{-t/T_2}r_{30}(\Delta)\{-\Delta\Omega_0\sin(k_x x)[1-\cos(\sqrt{\Omega_0^2+\Delta^2}t)]/(\Omega_0^2+\Delta^2)$$
$$+\Omega_0\cos(k_x x)\sin(\sqrt{\Omega_0^2+\Delta^2}t)/\sqrt{\Omega_0^2+\Delta^2}\}$$

By using these results in equations (6-4) and (6-5), we can find the output fields propagating in both directions as,

$$\Omega^+(t) = \Omega_0 + 0.5\alpha L e^{-t/T_2}w_0\Omega_0 J_0(\Omega_0 t) \tag{6-6}$$

$$\Omega^-(t) = 0.25\alpha L e^{-t/T_2}g_0\Omega_0[e^{-\Omega_0\tau_d}+J_0(\Omega_0\sqrt{t^2-\tau_d^2})-F(t)], \tag{6-7}$$

Where αL denotes the absorption length and $J_0(y)$ is the 0$^{\text{th}}$ order Bessel function. The calculation of $F(t)=\dfrac{2}{\pi}\int_0^-\dfrac{\Delta}{\Omega_0^2+\Delta^2}\cos(\sqrt{\Omega_0^2+\Delta^2}t)\sin(\Delta\tau_d)d\Delta$ still relies on numerical integration. However, the temporal patterns are already revealed in the expressions (6) and (7). The transmitted field, $\Omega^+(t)$, has a damped oscillatory term in the form of a Bessel function, which is the pattern of the typical optical nutation. The damping effects
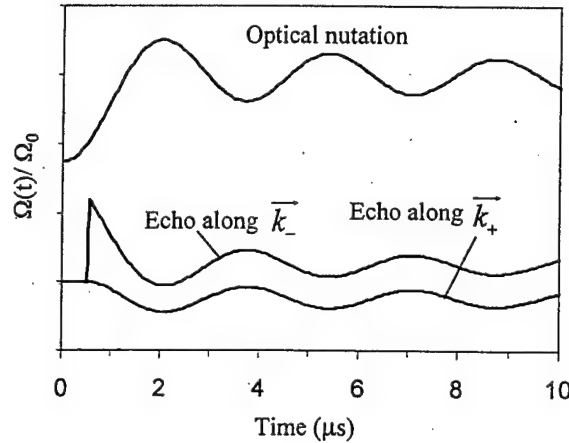

Fig. 6-2 Analytical results of the output fields from a SPE process in an optically thin medium with quasi-continuous probe fields. The transmission field and the echo fields in the causal, $\overrightarrow{k_-}$, and the non-causal, $\overrightarrow{k_+}$, directions are calculated from equations (6), (7), and (9), respectively, corresponding to the traces from top to bottom under the condition, $w_0 < 0$ and $w_0 = -g_0$, $\tau_d = 0.5$ μs, $\Omega_0 = 0.4$ MHz and $1/T_2 = 0$.

can be attributed to the coherent dephasing in the exponential term and the frequency detuning resulting the Bessel function. $\Omega^-(t)$ represents the echo field consisting of a DC term and two time-varying terms. Using expressions (6) and (7), we calculated the temporal shapes of the output fields with $\tau_d = 0.5$ μs, $\Omega_0 = 0.4$ and $1/T_2 = 0$. The transmitted field in $\overrightarrow{k_+}$ direction (equation (6-6)) is plotted in figure 6-2. The echo, described by equation (6-7), in the $\overrightarrow{k_-}$ direction is labeled as echo along $\overrightarrow{k_-}$ the same figure. Besides the typical optical nutation on the transmission, one can see that the delayed SPE also shows damped oscillation with the period determined by the probe Rabi

frequency. T_2 was assumed infinite in figure 6-2 to show the oscillations without the damping effect from the coherent dephasing. The nutation on both the transmission and echo is a direct result of coherent saturation becoming significant at a probe duration, τ_p $\gg \Omega_0^{-1}$.

The echo propagation direction is governed by phase-matching conditions and causality, which makes the asymmetrical diffraction from the spatial-spectral grating[9,10]. A typical brief pulse SPE can only exit the medium along $\overrightarrow{k_-}$ provided a brief probe is along $\overrightarrow{k_+}$. A brief probe along $\overrightarrow{k_-}$ will not generate any echo along $\overrightarrow{k_+}$. In that sense we call direction $\overrightarrow{k_-}$, along which the brief pulse echo propagates, the causal direction and $\overrightarrow{k_+}$, the non-causal direction. A continuous probe, however, gives different results. Setting a probe field along $\overrightarrow{k_-}$ and using equations (6-1) to (6-5) with a similar derivation, one can find the expressions of the output fields as,

$$\Omega^+(t) = 0.25\alpha L e^{-t/T_2} g_0 \Omega_0 [-e^{-\Omega_0 \tau_d} + J_0(\Omega_0 \sqrt{t^2 - \tau_d^2}) + F(t)], \qquad (6-8)$$

$$\Omega^-(t) = \Omega_0 + 0.5\alpha L e^{-t/T_2} w_0 \Omega_0 J_0(\Omega_0 t) \qquad (6-9)$$

While the transmitted field (10) is exactly the same as (6), a delayed echo (9) exists and now propagates through the medium in the non-causal direction. Figure 6-2 shows this echo along $\overrightarrow{k_+}$ direction having the same nutation period and the same DC level as the echo in the causal direction $\overrightarrow{k_-}$.

Experiments

The experiment, as shown in Figure 6-3, was designed to observe optical nutation and the nutational SPE's from a long probe and a preprogrammed medium. The laser source is a cw Ti: Sapphire laser frequency stabilized to a few tens of KHz by locking to a spectral hole in a Tm: YAG[11]. Two acousto-optic modulators (AOM) were used to generate programming and probe pulses on two beams. The two beams were overlapped, with an angle of ~0.05 radians, and focused to a spot of ~75μm (diameter at 1/e waist) in a Tm^{3+}:YAG crystal with an absorption length of 1.4. The AOM's also controlled the timing, direction and the power of the inputs. The duration of the two programming pulses was set to 100 ns each and the probe duration, τ_p was 10 μs. The delay between

the programming pulses, τ_d, was adjusted from 0.15 μs up to 2 μs to see the nutation effects of the delayed echoes. The direction of the first pulse was fixed to $\overrightarrow{k_+}$ and the second to for $\overrightarrow{k_-}$ all the experiments, which defined the causal and non-causal directions to be $\overrightarrow{k_-}$ and $\overrightarrow{k_+}$, respectively. The probe pulse was along one of these two directions to stimulate echoes in causul or non-causal directions. The peak power on each programming pulse was ~200mW while the probe was attenuated to a desired level between 7.6 to 200 mW by the AOM in the probe direction. Two photo diodes (PD) and a digitizing oscilloscope were used to measure and record the output powers as functions of time in both directions.
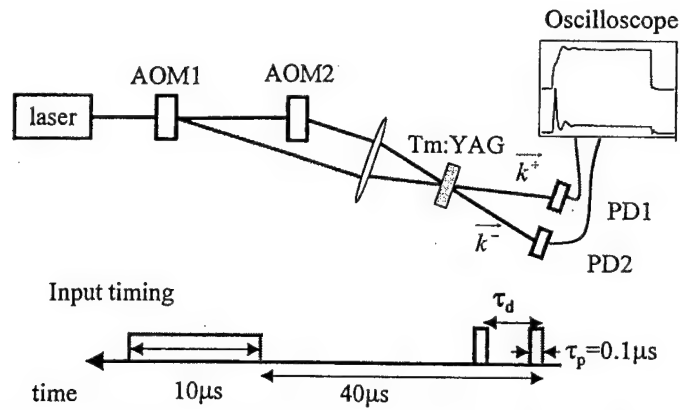
33

Fig. 6-3 Schematics of experimental setup and timing of the input pulses. The two programming pulses (0.1 μs each) are separated by a delay, τ_d, the first incident along $\overrightarrow{k_+}$ and the second along $\overrightarrow{k_-}$. The 10μs probe is set either along $\overrightarrow{k_+}$ to observe the echoes in the causal direction, $\overrightarrow{k_-}$, or along $\overrightarrow{k_-}$ to see the echoes in the non-causal direction, $\overrightarrow{k_+}$.

Results and discussions

In the first experiment, a 10 µs-long pulse with input power, P_p=28 mW was sent along $\overrightarrow{k_+}$ to probe the gratings with different delays. The transmission and the echoes for τ_d = 0.15, 0.3, 0.5, and 1,2 µs are plotted in figure 6-4. We see the nutation effects on both transmission and echoes as predicted. The echoes peak at τ_d after the leading edge of the probe, then start decaying as the probe field saturates the atomic population and oscillate with the atoms' Rabi oscillation. The peak echo power and the DC level decreases with τ_d. Figure 6-5 gives the echo efficiency varying with the probe power at fixed delay, τ_d = 0.15 µs. The high power corresponds to a high Rabi frequency and results in the fast oscillation and damping on the echo signal. The peak echo efficiency also deteriorates at high power.
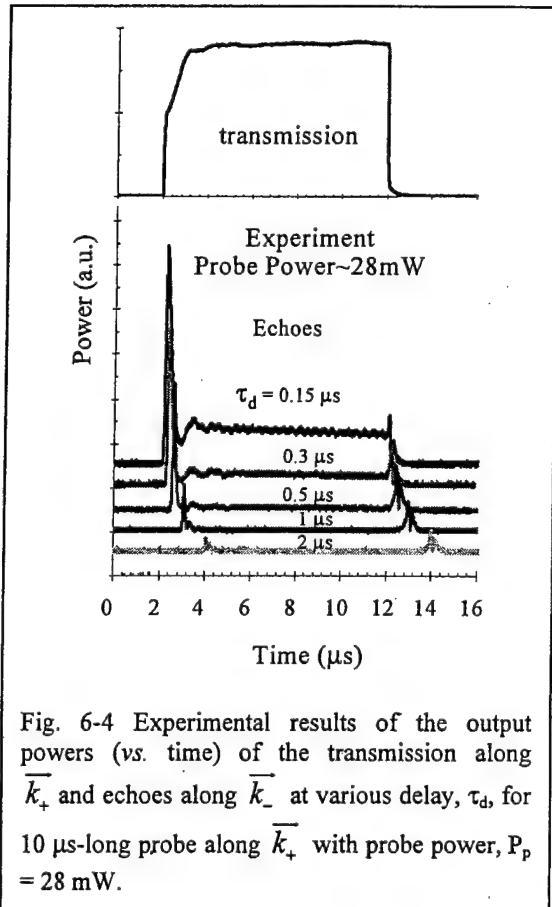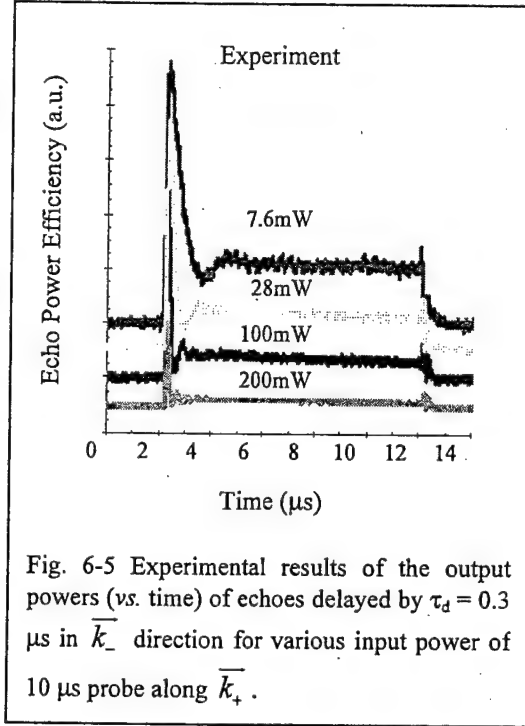

Fig. 6-5 Experimental results of the output powers (vs. time) of echoes delayed by τ_d = 0.3 µs in $\overrightarrow{k_-}$ direction for various input power of 10 µs probe along $\overrightarrow{k_+}$.

Fig. 6-4 Experimental results of the output powers (vs. time) of the transmission along $\overrightarrow{k_+}$ and echoes along $\overrightarrow{k_-}$ at various delay, τ_d, for 10 µs-long probe along $\overrightarrow{k_+}$ with probe power, P_p = 28 mW.
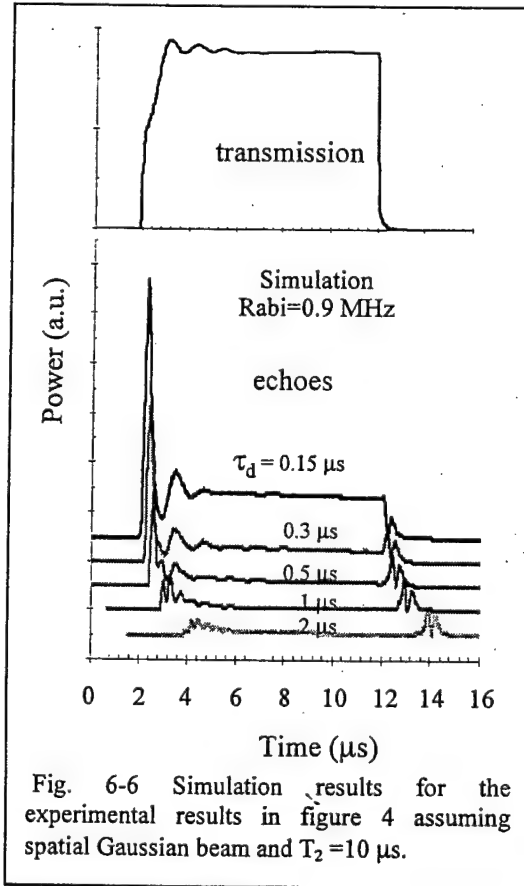

Fig. 6-6 Simulation results for the experimental results in figure 4 assuming spatial Gaussian beam and T_2 =10 µs.

35

These observations are consistent with the trends from the analytical solutions. However, the experimental results were obtained with the situation being more complicated than the simplified theory. The laser beam we used is a spatial Gaussian beam rather than a plane wave, which makes the optical power vary across the beam, and thus so does the Rabi frequency. We also used a crystal with an absorption length of 1.4 rather than a thin medium in order to obtain higher efficiencies. The absorption changes the optical power and the Rabi frequency as the field propagates and the echo output acts back to the medium. The damped oscillations of the echoes and the transmissions in the experiments are the collective effects of the local Rabi frequencies in the medium. This can be simulated by numerically solving the Maxwell-Bloch equation set (6-1)- (6-5) with various Rabi frequencies for plane wave fields and then doing weighted average of the output intensity according to a Gaussian distribution. Figure 6-6 gives the simulation results corresponding to the experiments in figures 6-4. From the optical nutations on the transmission in figures 6-4a, we can estimate the input probe Rabi frequency at the center of the Gaussian beam. According to reference[12], the Rabi frequency for figure 6-4a was estimated to $\Omega_0 \sim 0.8$ MHz assuming $\alpha L \ll 1$. The simulation results of the echoes at a higher Rabi frequency, $\Omega_0 = 0.9$MHz are a good fit to the experiment because of the absorption effect. Besides the coherent dephasing, the multi-Rabi components also cause the rapid damping to the DC level since the oscillations at different Rabi frequencies average out after the first few periods.

The second experiment is to switch the probe direction to $\overline{k_-}$ and monitor the output looking for an echo in the non-causal direction, $\overline{k_+}$. Figures 6-7 and 6-8 give the results under the same conditions as in figures 6-4 and 6-5, respectively, except the probe directions. The optical nutation was again observed on the transmission (figure 6-7). Comparing the transmission results in figure 6-7 with figure 6-4 one can see that the optical nutation on the transmissions in both directions are the same. Nutational echoes were also seen in the non-causal direction, in which a brief pulse SPE usually would not exist. The oscillations on the echoes in the non-causal direction are similar to those in the causal direction except the echoes start from zero power at delay, τ_d, after the leading edge of the probe. This experiment can also be simulated with the angled beam Maxwell-Bloch simulator. Figure 6-9 gives the simulation fit to the experimental results in figure 6-7. The two figures show good agreement between the theory and the experiment.
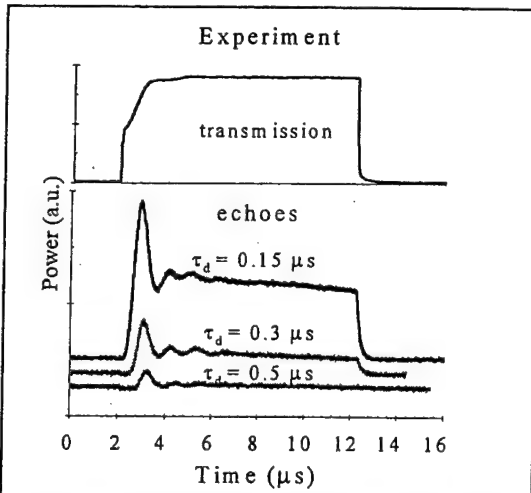
Fig. 6-7 Experimental results of the output powers (*vs.* time) of the transmission along $\overrightarrow{k_-}$ and echoes along $\overrightarrow{k_+}$ at various delay, τ_d, for 10 μs-long probe in direction $\overrightarrow{k_-}$ with probe power, P_p = 28 mW.
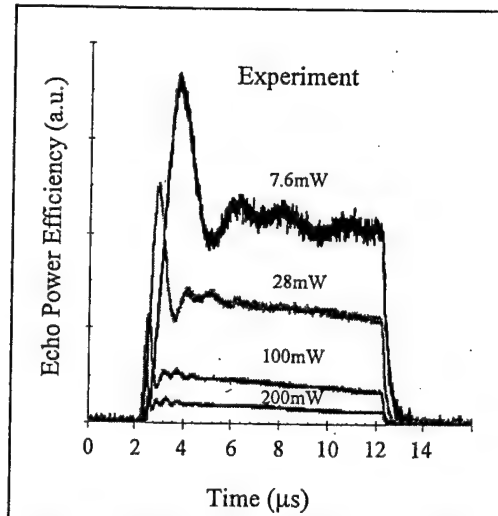

Fig. 6-8 Experimental results of the output powers (*vs.* time) of echoes delayed by τ_d = 0.3 μs in $\overrightarrow{k_+}$ direction for various input power of 10 μs probe along $\overrightarrow{k_-}$.
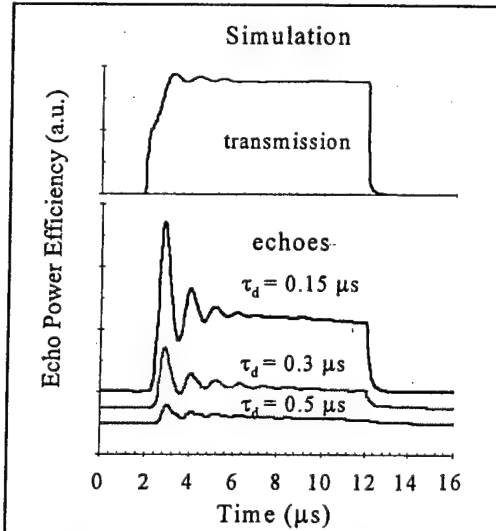

Fig. 6-9 Simulation results for the experimental results in figure 7 assuming spatial Gaussian beam and T_2 =10 μs.

The SPE from the long probe exiting in the non-causal direction does not violate the phase-match conditions or causality. The reason that an echo appears in the non-causal direction is
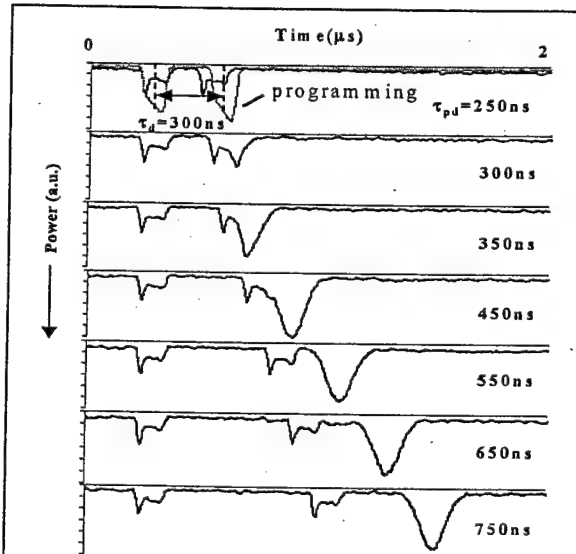
Fig. 6-10 Echo outputs in non-causal direction $\overrightarrow{k_+}$ from double pulse probe along $\overrightarrow{k_-}$ with various time separation τ_{pd} for a fixed delay, τ_d = 0.3 μs. The first two peaks of each trace are the scattered light from the probe, which show the timing of the probe pulses and can be used to compare with the timing of the programming pulses. The results show a causal echo can exist in the "non-causal" direction when the condition, $\tau_{pd} > \tau_d$, is satisfied.

37

that the probe pulse is longer than the delay τ_d. The front part of the probe pulse interacts with the grating and creates a coherence, which cannot generate a propagating field. However, the probe field incident into the medium anytime τ_d later than the front part re-phases this coherence into the propagating direction $\overrightarrow{k_+}$ and emits an echo. To demonstrate this, we did a third experiment. The first programming pulse was set along $\overrightarrow{k_+}$ and the second along $\overrightarrow{k_-}$ with a fixed delay, τ_d =0.3 µs. Two 100ns pulses separated by τ_{pd} were used as probes along $\overrightarrow{k_-}$. The output in the non-causal direction $\overrightarrow{k_+}$ was measured as τ_{pd} was increased from 0.25 µs up to 0.75 µs (shown in figure 6-10). The first two pulses in the traces are the scattered light from the probe pulses showing the time delay, τ_{pd}. The two brief probe pulses do not generate SPE's directly from the spatial-spectral grating in the non-causal direction because of the causality. This is seen in the two top traces where $\tau_{pd} < \tau_d$. The first probe, however, creates a coherence in the medium that rephases τ_d after the first probe along $2\overrightarrow{k_-} - \overrightarrow{k_+}$, but no field is allowed to propagate along that direction due to the phase matching condition. The second probe pulse interacts with this coherence to the second order and rephases it, similar to a two-pulse echo. When $\tau_{pd} > \tau_d$ ($\tau_{pd} > 300$ ns in figure 6-10 the rephased coherence generates a real echo along $\overrightarrow{k_+}$ at $\tau_{pd} - \tau_d$ after the second probe. This explains why a long quasi-continuous probe can create an echo in the non-causal direction where a brief probe cannot and the echoes in the "non-causal" direction, though unexpected, are causal.

References for section 6
[1] T. Mossberg, Opt. Lett. 7 (1982) 77
[2] V. V. Samartsev; V. A. Zuikov; L. A. Nefed'ev, J. Appl. Spectrosc. 59 (1993) 766.
[3] K.D. Merkel and W.R.Babbitt, Opt. Lett. 21 (1996) 1102.
[4] K. D. Merkel, Z.Cole, W.R.Babbitt, J. Lumin. 86 (2000) 375.
[5] G. B. Hocher and C. L. Tang, Phys. Rev. Lett. 21 (1968) 591.
[6] R. M. Macfarlane, and R. M. Shelby, in *Spectroscopy of Solids Containing Rare earth Ions,* edited. by A. A. Kaplyankii and R. M. Macfarlane (Elsevier Science Publisher B.V., New York, 1987), Chap 3.
[7] R. L. Shoemaker, in *Laser and Coherence Spectroscopy*, edited by J. I. Steifeld (Plenum Press, New York, 1978) Chap. 3.
[8] T. Chang, M. Tian, and W. R. Babbitt, To be published.
[9] S. Bernet, B. Kohler. A. Rebane, and A. Renn, and Urs P. Wild, J. Opt. Soc. Am. B 9 (1992) 987.
[10] Rebane, S. Bernet, A. Renn, and Urs P. Wild, Opt. Commun. 86 (1991) 7.
[11] N. M. Strickland, P. B. Sellin, Y. Sun, J. L. Carlsten, and R. L. Cone, Phys. Rev. B 62 (2000) 1473.
[12] Y. Sun, G. M. Wang, R. L. Cone, R. W. Equall, and M. J. Leask, Phys. Rev. B 23 (2000) 15443.

7. *Pulse Shaping Using Optical Coherent Transients*
This work is a spin-off from the achievements of this project. It leads to a new project currently funded through DEPSCOR. One peer-review journal paper has submitted and one conference talk has been accepted.

Optical coherent transient signal processing offers a novel method of optical pulse shaping at current optical communication bandwidths (GHz). Using multiple temporally-overlapped, frequency offset and phase-tuned, linear frequency chirps, we propose optical pulse shaping and processing in inhomogeneously broadened absorbers. Rare-earth doped crystals have the ability to perform pulse shaping in the frequency regime between the femtosecond pulse shaping and current analog electronics. Demonstrations of this pulse shaper on low bandwidths (~20 MHz) are shown. These include pulse train creation, self-convolution and auto-correlation, and chirped pulse compression.

Optical pulse shaping of femtosecond pulses has been thoroughly studied,[1] and applications such as coherent control of simple molecular processes have already utilized pulse shaping in experiments.[2] Other applications have been proposed such as production of dark solitons for long haul fibers, optical time domain multiplexing (OTDM), optical code-division multiple access (CDMA) multiplexing, and chirped pulse compression. Most methods of optical pulse shaping in the femtosecond to picosecond regime involve gratings to spatially disperse the frequency components of a pulse, which is then modulated using spatial light amplitude and phase modulators. Due to the limited resolution of gratings and spatial light modulators these techniques have frequency resolution of ~10 GHz making 100ps the maximum temporal duration of the pulse packet. Other methods of pulse shaping utilize beamsplitters and physical delay lines to create a desired temporal shape. These approaches have the disadvantage that it is very difficult to adjust or change the shape of the output pulse on a reasonable time scale. Previous investigations of picosecond pulse shaping have utilized spectral hole burning and the photon echo process in the organic materials,[3,4] but these results relied upon physical delays and could only achieve temporal durations ~100 ps. Very few methods of optical pulse shaping in the nanosecond regime exist.[5]

We report the proposal and proof-of-concept demonstration of pulse shaping using spectral hole burning and optical coherent transients (OCT) in inhomogeneously broadened absorbers such as rare-earth ion doped crystals. These crystals have inhomogeneous linewidths up to a 100 GHz, homogeneous linewidths as narrow as 1 kHz, and inhomogeneous to homogeneous ratios (time-bandwidth product) of 10^5-10^8. These crystals offer an excellent platform for pulse shaping in the gap between femtosecond pulse shaping techniques and the capabilities of electronics to create analog optical waveforms[5].

In previous works, we demonstrated experimentally that two temporally overlapped linear frequency chirped pulses (TOLFC) could be utilized to create periodic spectral gratings in rare-earth ion doped crystals.[7,8] A probe pulse incident upon this grating produces an echo output with a delay

$$\tau_d = \frac{\delta}{\alpha} \tag{7-1}$$

Here δ is the frequency offset between the two chirps and α is the chirp rate. The TOLFC method has many advantages over brief pulse programming and programming with two temporally separated linear frequency chirps. These advantages include chirp durations longer than the coherence time of the rare-earth ions, the ability to use a single chirp source for the programming pulses, and large delay tuning range (~µs) using small

frequency offsets (~MHz). With the development of high bandwidth (>40 GHz) chirped lasers the TOLFC method offers an attractive approach to high bandwidth OCT processing.[9,10] In this paper we propose a novel method utilizing multiple TOLFCs to produce complex spectral gratings for optical pulse shaping. This method offers a quickly adjustable (~ms), versatile, fully programmable way to perform pulse shaping in the picosecond to microsecond regime.

Using multiple frequency offset TOLFCs one creates several time delay gratings given by equation (7-1) instead of only one. Figure. 7-1a diagrams the multiple TOLFC programming method for use as a pulse shaper. A reference linear frequency chirp, $C_1(t)$, and control chirps, $C_2(t)$, with the desired frequency offsets are temporally and spatially overlapped in the inhomogeneous broadened material to create a complex spectral grating. Later the pulse to be shaped, $E_3(t)$, is diffracted off the grating producing multiple echoes. In general the desired output signal of a pulse shaper can be written in the form,

$$E_s(t) = \sum_{n=1}^{N} A_n b_a (t - n\tau) \qquad (7\text{-}2)$$

Here τ is the desired sampling period, A_n are complex amplitudes, and b_a is a temporally brief pulse with bandwidth, B_a. The output echo field of the stimulated photon echo process has a Fourier transform $E_s(\omega) \propto E_1^*(\omega) E_2(\omega) E_3(\omega)$, where $E_i(\omega)$ for i = 1, 2 and 3 are the spectra of the reference, the control and the probe fields respectively. By choosing the reference and the control pulses properly, a probe pulse can be shaped into an output pulse with an arbitrary shape. If the pulse to be shaped is brief, $E_3 = b_a(t)$, the action needed to create the desired output signal, $E_s(t)$, is equivalent to the creation of multiple delayed copies of the input pulse with the proper complex amplitudes. If the reference pulse is a linear frequency chirp, $C_1(t) \propto \exp(i\omega_1 t + i\frac{1}{2}\alpha t^2)$, of a bandwidth, $B \geq B_a$ with a chirp rate, α, and a start frequency, ω_1, then, the control pulse should take the form, $E_2 \propto \sum_n A_n C_1(t - n\tau)$, which is a superposition of delayed copies of the reference chirp weighted by A_n.

$$E_2(t) \propto C_1(t) \sum_{n=1}^{N} A_n \exp(-i\alpha n\tau t - i\omega_1 n\tau + i\frac{1}{2}\alpha (n\tau)^2) \qquad (7\text{-}3)$$

If the delays are much shorter than the chirp duration, the delays $(n\tau)$ can be replaced with frequency shifts of $n\delta = \alpha(n\tau)$ giving

$$E_2(t) \propto C_1(t) \sum_{n=1}^{N} A_n \exp\left(-in\delta t - i\omega_1 n\frac{\delta}{\alpha} + i\frac{(n\delta)^2}{\alpha} \right) \qquad (7\text{-}4)$$

This produces multiple TOLFCs with a different frequency offsets and weighted by complex amplitudes A_n. The additional phase term,

$$\phi_n = -\omega_1 \frac{n\delta}{\alpha} + \frac{(n\delta)^2}{\alpha} \qquad (7\text{-}5)$$

ensures the echo has the same phase regardless of delay, with relative phase between echoes controlled by A_n of each control chirp. In addition, the beam paths of reference chirp and the control chirps are angled, to separate the pulse shaped output from the probe and spurious echoes.
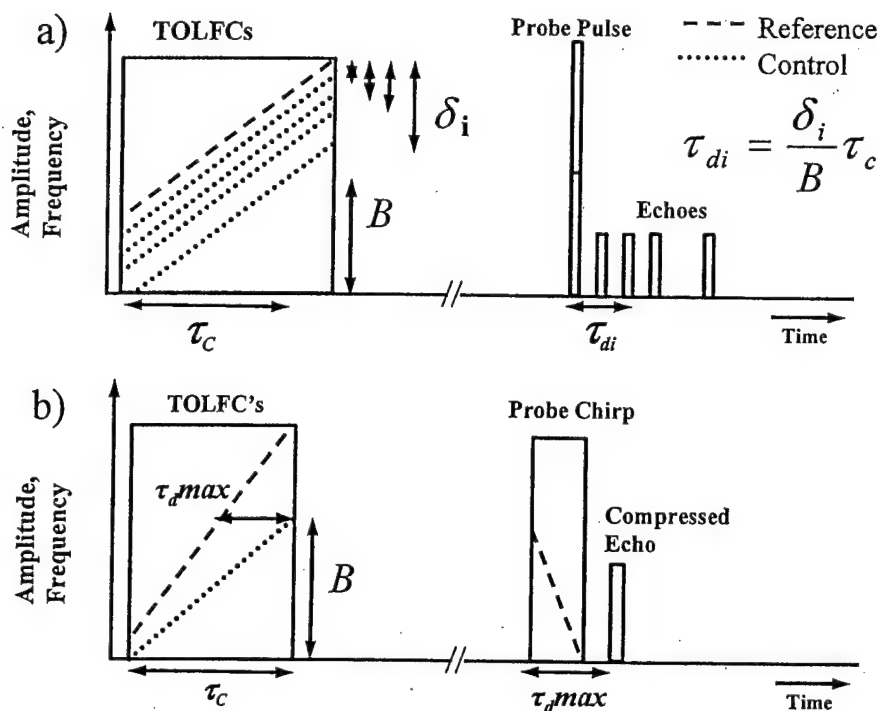
Fig. 7-1 (a) Schematic of the TOLFC pulse shaping process. Multiple linear frequency chirps with different starting frequencies (dotted lines) are temporally overlapped with a single higher frequency reference chirp (dashed line). Later a brief probe pulse is diffracted off the grating producing multiple echoes. In the real programming process, the maximum frequency offset is much less than the bandwidth of the chirps. (b) Schematic of the TOLFC chirp compression process. Two chirps with different chirp rates are temporally overlapped, creating a linearly chirped time delay grating that compresses the probe chirp to a delayed Fourier limited pulse.

The pulse shaper is not limited to shaping brief pulses. If an arbitrary input pulse is to be shaped into an arbitrary output with a given bandwidth and sampling rate, one only needs to work out the right set of the complex weighting factors, A_n, needed on the control pulse. For example, to turn the pulse train, $E_3(t) = \sum_{n=1}^{N} A_n b_a(t - n\tau)$, into its self-convolution, one can use the reference chirp and control pulses as discussed above. To get the auto-correlation the control pulse needed to create the time reverse of $E_3(t)$ in the basic pulse shaping process described above is used.

Another application of pulse shaping is chirped pulse compression. Previous studies have shown that OCT's have the ability to compress chirped pulses.[11,12,13] Here we show that the linear frequency chirps need not be temporally separate, and generalize chirp compression to the multiple TOLFC method. Chirp compression can be accomplished by using a reference chirp and a frequency offset control chirp with different chirp rates α_1 and α_2, respectively as shown in figure 7-1b. One can solve α_2 analytically if $|E_1(\omega)|$, $|E_3(\omega)|$ are uniform over the bandwidth of interest (i.e. large time bandwidth products). To compress the chirped pulse to its Fourier transform limit, $E_s(t) \propto b_a(t - \tau_d)$, one can set

41

the control chirp as, $E_2(\omega) \propto E_1(\omega) E_3^*(\omega) E_s(\omega)$, where $E_1(\omega) E_3^*(\omega)$ is equivalent to a linear frequency chirp with a chirp rate, $\alpha_2 = \frac{\alpha_1 \alpha_3}{\alpha_3 - \alpha_1}$. In the time domain, the control chirp then takes the form of $C_2(t) \propto \exp\left(i\omega_1(t-\tau_d) + i\frac{1}{2}\alpha_2(t-\tau_d)^2 \right)$, which is a temporally delayed chirp. Here τ_d is the delay time of the echo pulse with respect to the leading edge of the probe pulse and is confined to less than T_2 and greater than the probe chirp duration plus $1/B$. Since the delay is a function of the frequency, τ_d is also the delay of the probe chirp's start frequency. For the case of a limited time bandwidth product, the control chirp takes the same form, and the compressed pulse becomes a bandwidth limited delta function. For temporally overlapped reference and control chirps one can expand equation 7-1 to calculate the delay as a function of rf frequency ω, frequency offset δ, and chirp rates α_i as $\tau_d(\omega) = \frac{\omega}{\alpha_1} - \frac{\omega}{\alpha_2} + \frac{\delta}{\alpha_2}$. Using this method it should be possible to compress a multi-GHz chirp with a temporal duration of a few microseconds to its bandwidth limit.

Proof-of-concept demonstrations of the TOLFC pulse shaper for the different processes described above were done. Acoustic-optic modulators (AOM's) were used to create the linear frequency chirps, limiting these initial demonstrations to 20 MHz bandwidth. Experiments were performed using an external cavity diode laser with an injection locked amplifier lasing at the $^3H_4$-$^3H_6$ transition in Tm^{3+}:YAG (~793 nm).[14] The laser beam was split with a 50/50 beam splitter, passed through two separate AOM's driven by arbitrary waveform generators to create the reference and control chirps. The two beams were then focused and overlapped in the crystal cooled to ~4.5 K. Powers before the crystal were ~15mW on each path and the beams were focused into the crystal using a 75mm lens giving a spot diameter of ~60μm. The echo output of the pulse shaper was then incident onto an amplified silicon photodetector with 50 MHz of bandwidth. The RF waveform used to program the reference chirp was $\sin(2\pi f_1 t + \frac{1}{2}\alpha t^2)$ where f_1 is the start frequency of the chirp. The control chirps were frequency offset copies of this reference chirp.

First we tested the pulse shaper's ability to produce pulse trains with arbitrary times and phases. The goal was to program a complex spectral grating to produce the 11 bit Barker code (11100010010) at a 10 MHz data rate. Programming chirps were 5μs long with 20MHz bandwidth giving a chirp rate of 4MHz/μs. The frequency offset between control chirps needed to produce the 10 MHz sampling rate was 400kHz. The phase control was performed with (0.5), using a negative amplitude for control chirps corresponding to an echo with a π phase. Figure 7-2 shows the echo output from the 100ns probe pulse processed by the two different complex gratings producing the expected code in both a binary amplitude modulated coding (figure 7-2a) and a bi-phase $(0, \pi)$ coding (figure 7-2b). The phase encoding $(0,\pi)$ is observed by nulls in the output whenever there is a phase transition. Due to coherence dephasing effects the echo output amplitude usually decays exponentially with the delay time. To compensate, the relative amplitude of each chirp of the control pulse was adjusted to create uniform echo amplitudes across the data sequence[15].
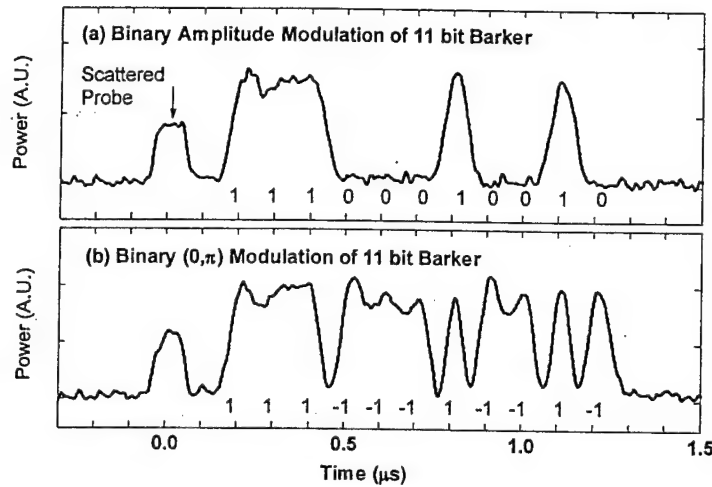
Fig. 7-2   The echo output of the pulse shaper probed with a 100ns pulse. Output is the binary representation of the 11 bit Barker code (11100010010) in (a) binary amplitude modulated (0,1) format and (b) a binary phase modulated (0,π) format.

Next we tested the ability of the pulse shaper to shape an arbitrary pattern. To demonstrate this we programmed the bi-phase 5-bit Barker code (1,1,1,-1,1) and the time-reverse (1,-1,1,1,1) versions of the code into the material. We then probed each grating with (1,-1,1,1,1), which yielded the operations of self-convolution and auto-correlation of the probe pulse, respectively. This is also an excellent test of the phase control of the pulse shaper. In the first experiment, only the intensity of the output waveform could be detected with only the nulls to suggest a phase flip. For correlation and convolution, phase is an important factor in determining the shape of the output. The theoretical outputs, with decay, are shown in figure 7-3 with the experimental convolution and correlation output of the pulse shaper.   The agreement between the experiment and calculated outputs confirms that we have phase control over the echo output. This scheme can be used to realize convolution and correlation operations between two arbitrary waveforms where one or both of the waveforms can be controlled.
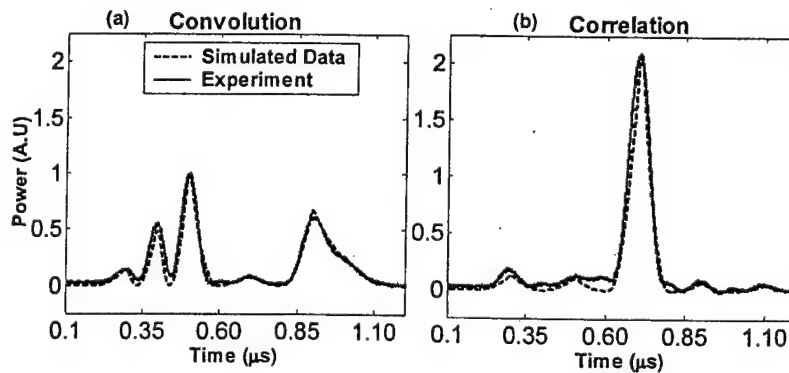

Fig. 7-3. The calculated and experimental output of the pulse shaper programmed with the (a) time reverse of the bi-phase 5 bit Barker code (1,-1,1,1,1) and (b) the time forward (1,1,1,-1,1) then probed with (1,-1,1,1,1) producing the self-convolution and the auto-correlation.

Finally we used this TOLFC pulse shaping method to perform linear frequency chirped pulse compression. A 1 µs pulse with a –20 MHz/µs chirp rate was to be compressed. For a 6µs long 20 MHz up chirped reference pulse, a chirp rate for the second chirp of 4 MHz/µs was required for compression. An offset of 0.3 MHz was added to the second chirped pulse giving a ~90ns delay between the end of the chirped probe and the echo. Figure 7-4 shows the probe chirp and the compressed echo output. The temporal width of the echo measured at ¼ the intensity was 64 ns. This gives a compression factor of ~16 with compressed echo duration close to the expected of 50 ns for a 20 MHz bandwidth limited pulse. As the chirped bandwidth of the pulses is increased, the compression factor should increase. This ability to compress chirps can also be combined with the basic multiple-TOLFC process described above by adding more control chirps creating multiple chirp compressing gratings with different time delays. By choosing the proper delays and phases of these compressed echoes and with the use of a high bandwidth chirp laser, high bandwidth analog optical signals and arbitrary waveforms can be created in the picosecond to microsecond regime.
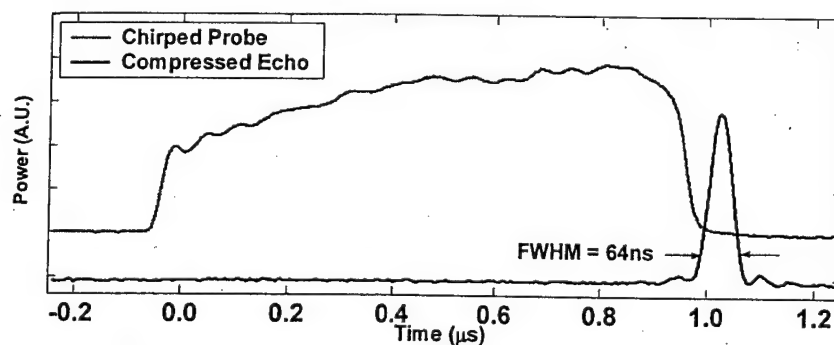

Fig. 7-4 Test of chirped pulse compression. A 1 µs, 20 MHz chirp was diffracted off a chirp compressing grating producing the narrow echo. The full width half max of the echo measured at one quarter the intensity is 64 ns, close to the bandwidth limit. The probe and echo are plotted on different scales.

We have demonstrated the ability to perform pulse shaping in rare-earth ion doped crystals using multiple, temporally overlapped linear frequency chirps. The versatility of this method was evident in its ability to not only shape brief pulses, but to perform pulse shaping on arbitrary signals, producing convolved outputs or compressed pulses. With the use of a high bandwidth chirped external cavity diode laser to create the chirps and AOM's to control the frequency offsets and phases, one could perform these processes at high bandwidths with low bandwidth electronics and low bandwidth acoustic-optic modulators.

References for section 7
[1] A.M. Weiner, Prog. Quant. Electr. **19**, 161 (1995).
[2] H. Kawashima, M.M. Wefers, and K.A. Nelson, Physica B. **219&220**, 734 (1996).
[3] H. Schwoerer, D. Erni, A. Rebane, and U.P. Wild, Optics Communications. **107**, 123 (1994).
[4] H. Schwoerer, D. Erni, and A. Rebane, J. Opt. Soc. Am. B. **12**, 1083 (1995).

[5] X. Ribeyre, C. Rouyer, F. Rauolt, D. Husson, C. Sauteret, and A. Migus, Optics Letters. **26**, 1173 (2001).

[6] R. L. Cone, R. W. Equall, Y. Sun, R.M. Macfarlane, and R. Hutcheson, Laser-Physics. **5**, 573 (1995).

[7] R. Reibel, Z. Barber, M. Tian, W.R. Babbitt, Optics Letters. **27**, 494 (2002).

[8] R. Reibel, Z. Barber, M. Tian, W.R. Babbitt, Journal of Photoluminesence. Accepted (2001).

[9] L. Ménager, L. Caberet, I. Lorgeré, and J.-L. Le Gouët, Optics Letters. **25**, 1246 (2000).

[10] L. Levin, Optics Letters **27**, 237 (2002).

[11] X. Wang, M. Afzelius, N. Ohlsson, U. Gustafsson, S. Kröll, Optic Letters. **25**, 945 (2000).

[12] Y.S. Bai and T.W. Mossberg, Optics Letters. **11**, 30 (1986)

[13] L. Ménager, I. Lorgeré, J.-L. Le Gouët, R. Mohan Krishna, and S. Kröll, Optics Letters. **24**, 927 (1999)

[14] R. Reibel, Z. Barber, M. Tian, W.R. Babbitt, J. Opt. Soc. Am. B. (To be published)

[15] K.D. Merkel and W.R. Babbitt, Optics Communications. **128**, 136 (1996)

8. *High Efficiency True-time-delay Echoes Using Linear Frequency Chirped Programming*

Compared with the brief pulse programming, linear frequency chirped programming is a more efficient programming method. In this section, echo power efficiencies are examined as a function of the pulse areas (or Rabi frequencies) of the programming, as well as a function of αL for TTD programming.

Figure 8-1 shows the various input sequences studied in this section. In (a) a data storage programming scheme is shown. This programming scheme was extensively studied by C. Cornish (see section above) and was the first programming scheme where greater than unit power efficiencies were predicted [1] and observed.[2] This scheme is studied here as a check on the new Maxwell-Bloch simulator for large αL. Here, the first pulse in the sequence is a brief pulse with a significant pulse area, θ_1. The second pulse in the sequence is known as a data pulse, and has a bandwidth less than the first pulse and also has low pulse areas, θ_2. Finally, at a later time, the stored data can be recalled by a probe pulse identical to the first pulse with a significant pulse area, θ_P, stimulating an echo representative of the data pulse.

This sequence was simulated using the Maxwell-Bloch simulator, with the same parameters found in the work done by C. Cornish.[3] The power efficiency is plotted as a function of αL for various $\theta_1 = \theta_P = A$, ranging from 0.1 π to 0.7 π in figure 8-2. Here the first and third pulses were Guassian with FWHM's of 0.1 ns. The data pulse was also Guassian and had a FWHM of 0.4 ns and $\theta_2 = 0.01 \pi$. As can be seen in the plot, efficiencies greater than unity are predicted around $\alpha L = 3$ for A > 0.6 π. This figure is in excellent agreement with the study shown in ref. 3, where analytic and simulated results are shown, suggesting that this new simulator is working and producing the expected results for thick αL.
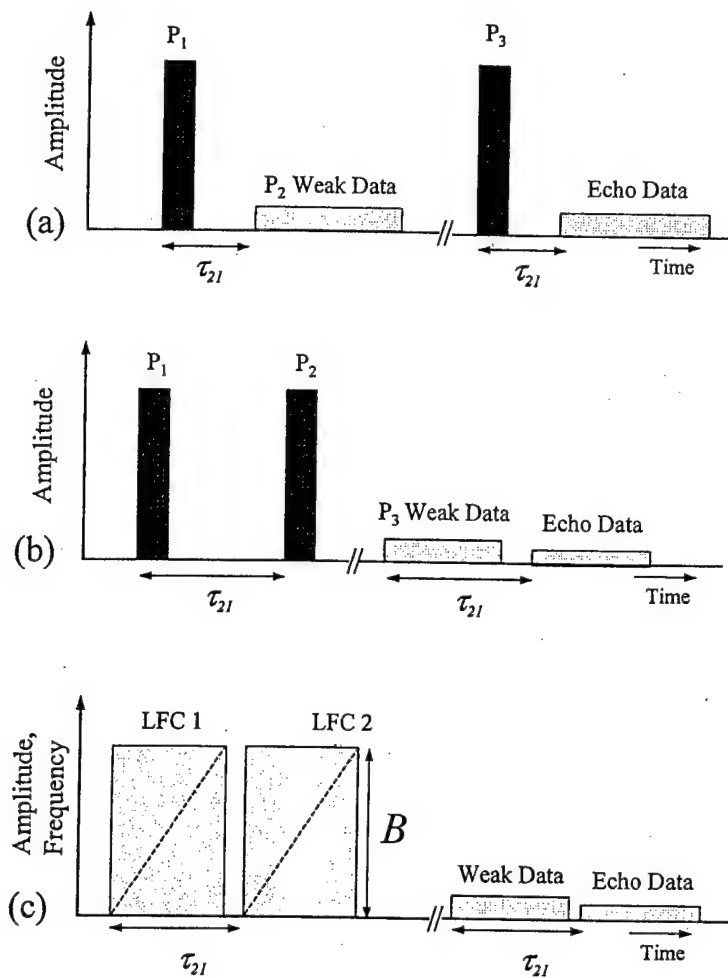
45

Fig. 8-1 Illustrations of each of the simulated input sequences studied for this thesis. In (a) a data storage configuration is shown. This configuration has shown better than unit efficiencies (see above section on echo efficiency) and is simulated here for comparison with new arbitrary phase Maxwell-Bloch simulator. (b) A brief programming pulse scheme for programming TTD. (c) A linear frequency chirped programming scheme for producing TTD.

While work had been done on the data storage sequence, there has been no discussion of the power efficiencies for TTD sequences. As was stated in chapter 2, TTD can be created using brief pulses or with chirped pulses. Figure 8-1 (b) shows an example of programming TTD using brief pulses. Now, two brief pulses, of significant pulse areas $\theta_1 = \theta_2$, write a spectral grating into the medium, then an arbitrary data pulse, with a low pulse area, θ_p, and low bandwidth compared to the brief pulses, probes the grating, stimulating a TTD version of itself.
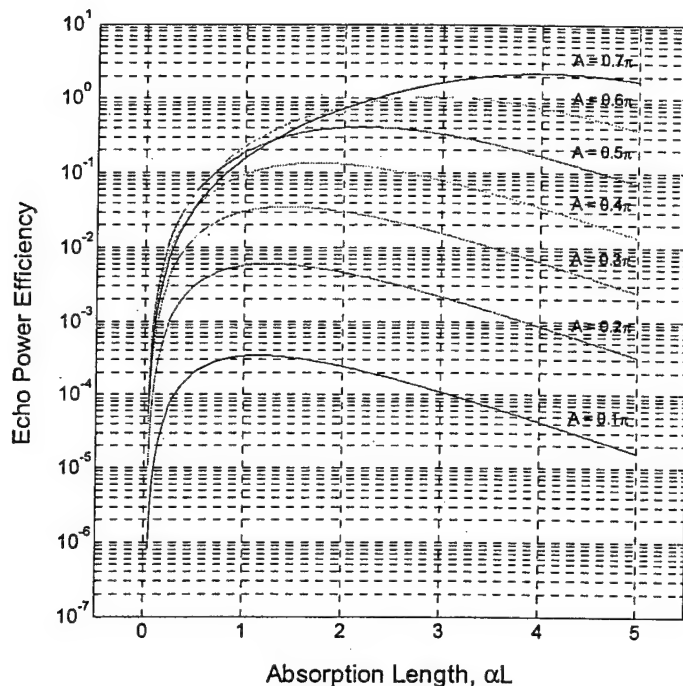
Fig. 8-2 Power efficiencies for the data storage programming scheme shown in figure 8-1 (a). Here $\theta_1 = \theta_p = A$ and range from 0.1 to 0.7 π. The first and third pulses were Guassian with FWHM's of 0.1 ns. The data pulse was also Guassian and had a FWHM of 0.4 ns and $\theta_2 = 0.01\pi$.

The power efficiencies for the brief pulse TTD programming sequence are shown in figure 8-3. In this simulation, $\theta_1 = \theta_2 = A$ and range from 0.1 to 0.9 π. The first and second pulses were Guassian with FWHM's of 0.1 ns. The data pulse was also Guassian and had a FWHM of 0.2 ns and $\theta_p = 0.05$ π. It can be seen in this figure that the echo efficiency peaks around an $\alpha L = 2.3$, with a maximum efficiency of 33% for A = 0.5 π. This is a significant efficiency, compared to thin αL's where efficiencies of 0.1-2% are common. Thus, as previously demonstrated for the programming data sequences, highly efficient photon echoes can be produced for optically thick crystals. Unlike the data storage case, shown in figure 8-1(a), efficiencies for TTD are still less than unity.
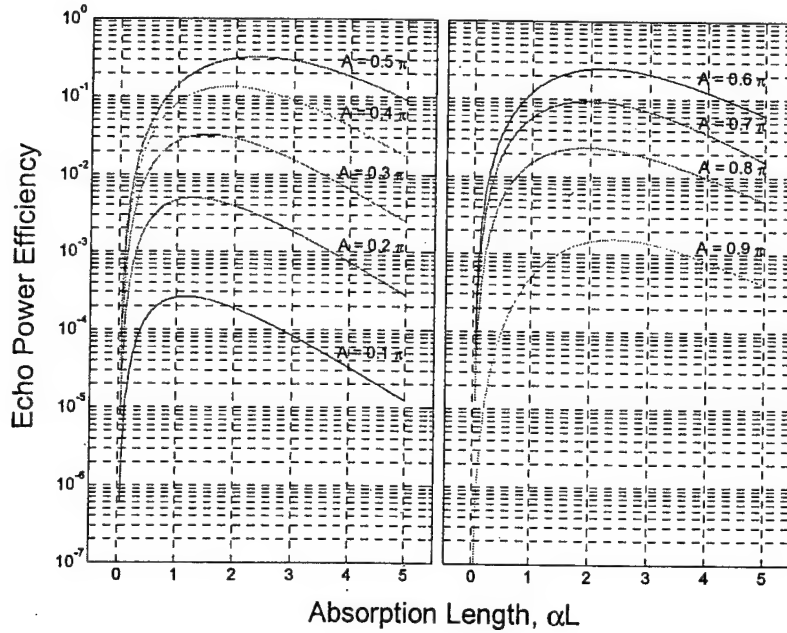
47

Fig. 8-3 Power efficiencies for the brief pulse TTD programming scheme shown in figure 8-1 (b). Here $\theta_1 = \theta_2 = A$ and range from 0.1 to 0.9 π. The first and second pulses were Guassian with FWHM's of 0.1 ns. The data pulse was also Guassian and had a FWHM of 0.2 ns and $\theta_P = 0.05$ π.

Now, the attention is turned to the linear frequency chirped programming sequence. In this case, as shown in figure 8-1(c), the first two programming pulses are now linear frequency chirps. It is difficult to discuss pulse areas when talking about linear frequency chirps as their frequencies are chirping unlike the brief pulse case. Instead these pulses are characterized by their bandwidths (B), durations (τ_C) and Rabi frequencies (Ω). In this case, the power efficiencies are examined as a function of the absorption length and the Rabi frequency, keeping the bandwidth and duration constant. Like the brief pulse case, the two linear frequency chirps are energetically strong, with $\theta_1 = \theta_2$, and write a spectral grating. Then an energetically weak data probe stimulates the grating producing a TTD version of itself.

The power efficiencies for the chirped case are plotted in figure 8-4 Here $\theta_1 = \theta_2 = \Omega$ and ranges from 5 GRad/s to 19 GRad/s. The programming bandwidth was $B = 50$ GHz and τ_C ns. The data pulse was Guassian and had a FWHM of 0.04 ns and $\theta_P = 0.05$ π. Here the power efficiency can be seen to peak around an $\alpha L = 3.0$ with a maximum power efficiency of 62% for $\Omega = 12$ GRad/s. It is interesting to note, that using

$$\Omega_{eq} = 0.267\sqrt{\frac{B}{\tau_C}} ,$$

the $\pi/2$ equivalent Rabi frequency is calculated to be $\Omega_{eq} = 11.8$ GRad/s. This is in close agreement with the value for the peak efficiency Rabi of 12 GRad/s. This suggests that,

as was the case for the brief pulses, that pulses with areas close to π/2 program the most efficient gratings and give the highest power efficiencies for TTD. The power efficiency of 62% is approximately twice as large compared to the brief pulse programming sequence. This result suggests that linear frequency chirped pulse programming can be highly efficient, which is good news for applications such as TTD beam steering for phased array radar. This along with other advantages discussed later, make linear frequency chirped programming an attractive avenue for practical operation.
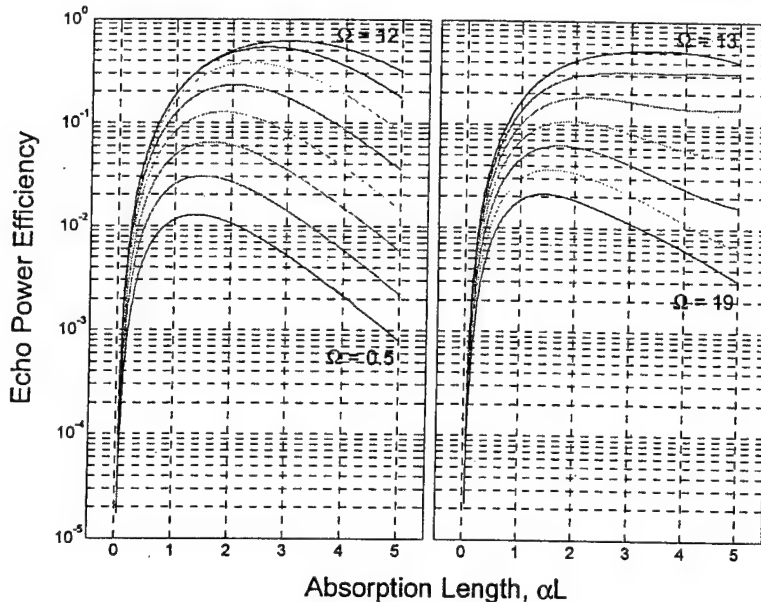

Fig. 8-4 Power efficiencies for the linear frequency chirped pulse TTD programming scheme shown in figure 8-1(c). Here $\theta_1 = \theta_2 = \Omega$ and ranges from 5 GRad/s to 19 GRad/s. The programming bandwidth was $B = 50$ GHz and $\tau_C = 1$ ns. The data pulse was Guassian and had a FWHM of 0.04 ns and $\theta_P = 0.05$ π.

Finally, to ensure that these efficiencies would hold for arbitrary data pulses, a data sequence was used. This data sequence was a bi-phase, amplitude modulated sequence. Here, the data pulses had bit lengths (FWHM's) of 0.04 ns and individual pulse areas of 0.02 π. The seven bit input sequence was +π/4, -π/4, +π/4, 0, π/4, 0, -π/4, where 0 represents zero amplitude and the amplitude for the other bits is constant, whereas the phase of the bits can range from ± π/4. The programming pulses had an W = 12 GRad/s, $\tau_C = 1$ ns, $B = 50$ GHz, and a programmed time delay of $\tau_D = 1.5$ ns. Figure 8-5 shows the input probe pulse (dotted line) and the output at an αL = 3.06 (solid line). An extremely high efficiency of 58% can be seen. The phase of the output bits was measured at the center of each bit and were found to be 0.90, -0.71, 0.82, 0, 0.85, 0,-0.75,0. The largest deviation from the expected value of π/4 is the first bit, which gives a percent error of ~14%. Overall, good fidelity can be seen, suggesting that the linear frequency chirped programming method will be useful for practical applications that require high power efficiencies.
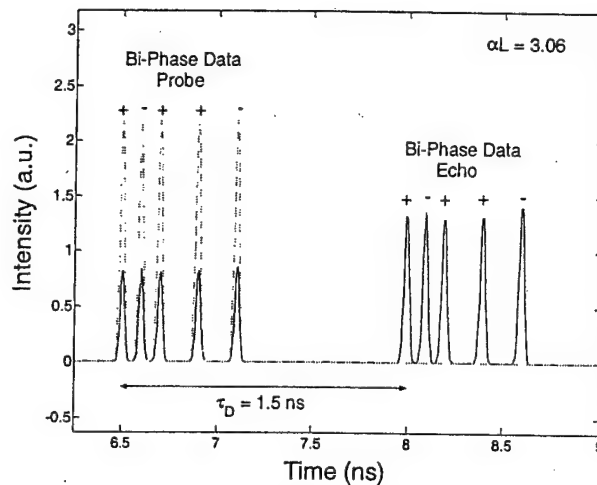
49

Fig. 8-5 A simulation of bi-phase, amplitude modulated data undergoing highly efficient TTD. The input is the dotted line. The solid line is the output at $\alpha L = 3.06$ where the efficiency is close to 60%. This is approximately twice the efficiency from the brief pulse programming scheme. Here the bits had FWHM's = 0.04 ns and $\theta_{bit} = 0.02$ π. The programming chirps had $\pi/2$ equivalent $\Omega = 12$ GRad/s, $B = 50$ GHz, and $\tau_C = 1$ ns.

References for section 8

[1] M. Azadeh, C. S. Cornish, W. R. Babbitt and L. Tsang, Phys. Rev. A **57**, 4662-8, 1997

[2] C. S. Cornish, W. R. Babbitt and L. Tsang, Ops-Lett. **25**, 1276-8, 2000.

[3] C. Cornish, Highly Efficient photon echo generation and a study of the energy source of photon echoes, PhD Thesis, University of Washington, 2000.

9. Control of Geometric Phase in OCT systems

When a quantum system evolves along a cyclic route, it acquires a geometric phase. Different from the Hamiltonian-dependent dynamic phase the geometric phase depends only on the circuit path itself[1]. Geometric phase has been observed in spin ½ systems through nuclear magnetic resonance experiments[2] and with polarized photons using interferometers[3]. Recently, the topic of geometric phase has been attracting increasing interest because of its importance for understanding and implementing quantum computation in real physical systems. It has been suggested the geometric phase to be used to realize C-not logic gate operations in spin 1/2 systems[4], and in superconducting nanocircuits[5]. On the other hand, atomic systems, such rare-earth ions doped in crystals, have been proposed as possible physical systems to realize quantum computation[6]. Study of the geometric phase in these systems will be of significance for understanding the physical processes governed by quantum theory, as well as application issues, such as the preparation and the operation of the atoms as qubits. As a first step towards physical implementation of quantum computation in such a material, we report an experimental demonstration of the optical control of the geometric phase in an atomic system of Barium vapor that has properties similar to those of rare-earth ion doped systems.

As an optical analog of a spin 1/2 system driven by a magnetic field, a two-level atomic system driven by an electromagnetic field can undergo a cyclic evolution. The

geometric phase of the system then depends upon the closed loop traced by the atomic state vector (the Bloch vector), in the projective Hilbert space (the Bloch sphere). Precisely, the geometric phase is equal to half of the solid angle subtended by the Bloch vector undergoing the cyclic evolution[2]. For example, if the electromagnetic field acting on the atoms has a pulse area of 2π, the Bloch vector evolves through one full revolution cycle enclosing a solid angle of 2π provided decoherence is ignored during the interaction. During this cyclic evolution, the atomic wave function therefore gains a geometric phase of π. In order to bring the system back to its original state, a pulse with area of 4π is needed to impart a geometric phase of 2π on the final wave function. It has been suggested that such electromagnetic control of the geometric phase can be observed using photon echo experiments under the condition that the two atomic levels are coupled to a third level[7].

In this section, we report to the best of our knowledge the first observation of the electromagnetic control of geometric phase in a three-level atomic system. The phase change of the atomic wave function was measured with photon echoes in Barium vapor. The Barium transitions used were between the $^1S_0$ (ground state) and triplet $^3P_1$ (excited states) as shown in figure 9-1 (a). The Zeeman levels of the $^3P_1$ were split by an external magnetic field applied parallel to the optical propagation direction. The $m = \pm 1$ Zeeman levels, $|+\rangle$ and $|-\rangle$, together with the ground state, $|g\rangle$ constituted a V type three-level system[8]. The transition between the m=+1 Zeeman level and the ground state is excited by right-hand circularly polarized ($\sigma+$) light, while the m=-1 Zeeman level responds to left-hand polarized ($\sigma-$) light.

A typical photon echo is produced in a two-level system, for example the two level system created by $|g\rangle$ and $|-\rangle$, by applying two resonant light pulses in sequence. The first pulse creates a coherence between $|g\rangle$ and $|-\rangle$ that dephases after the first pulse due to the inhomogeneous Doppler broadening of the transition. The second pulse, which happens at a time τ_{21} after the first pulse, rotates the phase of the atoms about π, resulting in a rephasing of the coherence for all atoms, regardless of detuning, at time $2\tau_{21}$. This rephasing results in an echo pulse, which is in phase with the laser, provided the two pulses have the same phase.

For a two-level system, $|g\rangle$ and $|-\rangle$, the atomic wave function at any point in time can be written as, $\Psi(t) = c_g(t)|g\rangle + c_-(t)|-\rangle$. The observable is the macroscopic polarization that has an expectation value calculated as $P_{g-}(t) = \langle \Psi(t)|\mu_{g-}|\Psi(t)\rangle = (c_g c_-^* + c_- c_g^*)\mu_{g-}$, where μ_{g-} is the atomic dipole moment associated to $|g\rangle$ and $|-\rangle$ transition. If $\Psi(t)$ undergoes a cyclic circuit C in a closed system, for instance by applying optical driving fields with pulse areas, $\theta = 2n\pi$, where n is integer number, the Bloch vector encloses a solid angle of θ provided the coherent dephasing is negligible during the evolution (the pulse duration is considered to be much shorter than one over the detuning from the laser of the atom of interest). The wave function acquires a geometric phase, $\phi_c = \theta/2 = n\pi$, and $\Psi(t)$ is multiplied by $\exp(i\phi_c)$. However, the geometric phase change in such a two level system is undetectable by measuring the observable $P_{g-}(t)$, as the phase terms simply cancel.

Next consider the wave function of the three-level system given by $\Phi(t) = c_g(t)|g\rangle + c_-(t)|-\rangle + c_+(t)|+\rangle$. If the transition between $|g\rangle$ and $|+\rangle$ undergoes a cyclic circuit D, then $\Phi(t) = \exp(i\phi_D)c_g(t)|g\rangle + c_-(t)|-\rangle + \exp(i\phi_D)c_+(t)|+\rangle$. The resultant phase change is observable in the polarization between $|g\rangle$ and $|-\rangle$ any time afterwards as $P_{g-}(t) = \{\exp(i\phi_D)c_g c_-^* + \exp(-i\phi_D)c_- c_g^*\}\mu_{g-}$. Thus, the sign of the echo field depends upon the accrued geometric phase. If the $|g\rangle$ to $|+\rangle$ transition is driven by an optical pulse with an area of $\theta = 2n\pi$, the geometric phase accrued is $n\pi$, resulting in observable echo field phase changes of $(-1)^n$. Thus, the optically induced geometric phase changes can be observed by measuring the phase changes of the echo fields.

Figure 9-1 (b) shows the schematic of the experimental setup. A cw Ti: Sapphire laser at 791nm was resonant with the $^1S_0$ - $^3P_1$ transition. The two $^3P_1$ Zeeman levels ($m = \pm 1$) were split by 205MHz using an external magnetic field of 49.4 Gauss applied along the propagation direction of the light. The two acoustic-optical modulators, AOM 1 and AOM 2 were used to create and control the timing, the frequencies and the amplitudes of the optical pulses. This was done so that the optical pulses on beams 1 and 2 were resonant with $|g\rangle$-$|-\rangle$ and $|g\rangle$-$|+\rangle$ transitions, respectively, as well as to control the individual pulse areas. The half-wave and the quarter-wave plates were orientated such that the beams had the polarization needed to excite the corresponding transitions. The timing and the polarization of the pulses are illustrated in figure 9-1(c). Two input pulses on beam 1 with pulse areas of $\pi/2$ and π, respectively, resonant with the $|g\rangle$-$|-\rangle$ transition were used to generate the echo signal. A driving pulse on beam 2 was tuned to excite $|g\rangle$-$|+\rangle$ transition. The driving pulse was applied between P1 and P2 and its pulse area was adjusted by varying the amplitude with AOM 2. The coherent dephasing time was measured to be 1.6μs under these experimental conditions. The two input pulses and the driving pulse durations were 0.15 μs or less. Thus the coherent dephasing can be essentially ignored during the pulses. The coupling condition of the three-level system was tested and the results are plotted in figure 9-2. The three out-of-scale pulses in the plot indicate the two input and driving pulses. Trace 1 shows the echo with applied magnetic field, B = 49.4 Guass for zero pump power and trace 2 for zero applied magnetic fields with pump pulse, $\theta = \pi$. In both cases, the two Zeeman levels were not coupled. In the first case, the pump pulse was non-existent therefore no atoms were excited to the third level. In the second case, the pump pulse was associated with far detuned atoms because there was no splitting of $m = \pm 1$ levels. Without the coupling the atoms can be considered as isolated two-level systems. The echoes should not be affected by the presence of either the driving pulse or the magnetic field alone. When the driving pulse is applied with the magnetic field, the two Zeeman levels are then coupled through the ground state by the input and driving pulses. When the driving pulse area is π, as shown in trace 3 of figure 9-2, the echo intensity is minimized because most of the atoms are pumped up to $|+\rangle$ from the ground state, $c_g = 0$, thus, $P_{g-} = 0$ and no echo is emitted. This ensures that the system is properly coupled.

With the three-level system consisting of two coupled Zeeman levels and a common ground state, we studied the driving pulse's effect on the relative phases of the echo fields

to observe the geometric phases induced by the driving pulses with different pulse areas. In order to observe the echo phase change we used a low intensity, long reference pulse to homodyne with the echoes. Figure 9-3 (a) show the echoes for 0, π, 2π, 3π and 4π driving pulses as marked on the corresponding traces. The bottom trace shows only the reference pulse. A 2π driving pulse results in a π phase shift on the echo field with respect to the case of having no driving pulse, conclusively demonstrating the half integer nature of the geometric phase of the atomic state after one full cyclic evolution of the Bloch vector. The echo with a 4π driving pulse has the same sign as that with zero driving field as expected returning the wave function to its initial state. One noticeable feature is that the pump pulse caused the echo delay τ_{21} to shift. This is due to the non-negligible duration of the driving pulse causing a temporal duration for the cycling of the atoms, which affects the echo rephrasing timing. The transit stages of the evolution driven by driving pulses with areas of π and 3π are more complicated since the echo fields also associate with dynamic phase changes.

In order to evaluate the effects of the delay shifts and the transit stages we adapted the theory in ref. 9 to model the photon echo process in a coupled three-level system. The density matrix in the atomic frame, $\rho(t,\Delta) = \begin{pmatrix} \rho_{gg} & \rho_{g-} & \rho_{g+} \\ \rho_{-g} & \rho_{--} & \rho_{-+} \\ \rho_{+g} & \rho_{+-} & \rho_{++} \end{pmatrix}$, keeps track of the atomic movement at time, t, and detuning, Δ. The detuning is defined as the atomic transition frequencies minus the corresponding laser frequencies by assuming the two laser frequencies are on resonance to the same atoms. The interaction matrix for the excitation resonant between $|g\rangle$-$|-\rangle$, as the two input pulses are, is

$$M_n(\Delta) = \exp(-i\Delta\tau_n/2) \begin{pmatrix} \cos(\frac{\theta_n}{2}) + \frac{i\Delta}{\Omega_n}\sin(\frac{\theta_n}{2}) & \frac{i\Omega_{n0}}{\Omega_n}\sin(\frac{\theta_n}{2})e^{i\Delta(t_n+\tau_n)} & 0 \\ \frac{i\Omega_{n0}}{\Omega_n}\sin(\frac{\theta_n}{2})e^{-i\Delta t_n} & \cos(\frac{\theta_n}{2}) - \frac{i\Delta}{\Omega_n}\sin(\frac{\theta_n}{2})e^{i\Delta\tau_n} & 0 \\ 0 & 0 & 1 \end{pmatrix},$$

where n=1,2 corresponding to pulses 1 and 2, respectively. $\Omega_{n0} = \mu E_n/\hbar$ and $\Omega_n = \sqrt{\Omega_{n0}^2 + \Delta^2}$ denote the on-resonant and generalized Rabi frequencies for a constant electric field, E_n and frequency detuning, Δ. The pulse area is defined as, $\theta_n = \Omega_n\tau_n$, for pulse duration, τ_n. t_n is the start time of the nth pulse. Similarly, the interaction matrix of the driving pulse that excites $|g\rangle$-$|+\rangle$ transition, is

$$M_p(\Delta) = \exp(-i\Delta\tau_p/2) \begin{pmatrix} \cos(\frac{\theta_p}{2}) + \frac{i\Delta}{\Omega_p}\sin(\frac{\theta_p}{2}) & 0 & \frac{i\Omega_{p0}}{\Omega_p}\sin(\frac{\theta_p}{2})e^{i\Delta(t_p+\delta_p)} \\ 0 & 1 & 0 \\ \frac{i\Omega_{p0}}{\Omega_p}\sin(\frac{\theta_p}{2})e^{-i\Delta t_p} & 0 & \cos(\frac{\theta_p}{2}) - \frac{i\Delta}{\Omega_p}\sin(\frac{\theta_p}{2})e^{i\Delta\delta_p} \end{pmatrix}.$$

These formulas for the interaction matrices are valid under the condition that none of the pulses are temporally overlapped and the homogeneous dephasing is ignored. The atomic state after interacting with two input pulses and a driving pulse applied in between can be calculated as,

$$\rho(t_2 + \delta_2, \Delta) = M_2(\Delta) M_p(\Delta) M_1(\Delta) \rho(t_1, \Delta) M_1^+(\Delta) M_p^+(\Delta) M_2^+(\Delta).$$

Where M^+ is the Hermite conjugate of M and the initial state is usually set to,

$\rho(t_1, \Delta) = \begin{pmatrix} 1 & 0 & 0 \\ 0 & 0 & 0 \\ 0 & 0 & 0 \end{pmatrix}$. The electric field of the echo signal is proportional to the induced

macroscopic polarization, which itself is proportional to the inverse Fourier transform of

$\rho_{g-}(\Delta)$ as $E_{echo}(t) \propto \int_{\infty}^{-\infty} \rho_{g-}(\Delta) \exp(i\Delta t) d\Delta$, assuming a uniform spectral distribution of

the atoms. Figure 9-3(b) plots the calculated echo fields corresponding to the experimental conditions in figure 9-3(a). The calculated echo shapes show good agreement with those measured in the experiment. The delay shifts of the echo measured and calculated for a driving pulse with area of 2π are ~60ns. The delay shift caused by a 4π driving pulse is the same as the 2π driving pulse since both pulses have the same duration. A driving pulse with area of π or 3π does not result in a zero echo field because of the contributions from the off-resonant atoms. The echo strengths when a pump pulse is applied are smaller in the experiment than those of the calculation. This is likely due to the non-uniformity of the Rabi frequencies in the experiment because of the Gaussian spatial profile of the laser power across the beam as well as absorption of the pulse along the direction of propagation.

In conclusion, we have observed the optical control of geometric phase for an atomic state using photon echoes. The experiment required a coupled three-level system, in which the pump laser was resonant to a two-level subsystem while the echo was observed in a different two-level subsystem. Results showed that pump pulses with areas of 2π and 4π resulted in geometric phases of π and 2π, respectively. The calculated and observed echo field shapes and phases are in good agreement with each other. Although the experiment was performed in Barium vapor, a similar experiment can be conducted in solid state atomic systems such as rare-earth doped crystals. This class of materials is a possible physical system for quantum computing, and further studies could be performed to realize universal operations based on a single qubit and C-not gates through optical manipulation of the geometric phase.

References for section 9
[1] S. Pancharatnam, Proc. India Acad. Sci. A **44**, 247 (1955); Y. Aharonov and Bohm, Phys. Rev. **115**, 485 (1959); M. V. Berry, Proc. R. Soc. A **392**, 45 (1984); Y. Aharonov and J. Anandan, Phys. Rev. Lett. **58**, 1593 (1987).
[2] D. Suter, K. T. Mueller, and A. Pine, Phys. Rev. Lett. **60**, 1218 (1988).
[3] R. Bhandari and J. Samuel, Phys. Rev. Lett. **60**, 1211 (1988); R. L. Chiao, et al., Phys. Rev. Lett. **60**, 1214 (1988).
[4] X. Wang and K. Matsumoto, J. Phys. A, **34**, L631 (2001).
[5] G. Falci, et al., Nature **407**, 355 (2000).

[6] M. D. Lukin, and P.R. Hemmer, Phys. Rev. Lett. **83**, 2818 (2000); M. S. Shahriar, et. al. Opt. Comm. **195**, 411 (2001); N. Ohlsson, R. K. Mohan, and S. Kroll, Opt. Comm. **201**, 71 (2002).

[7] T. Sen and J. L. Milovich, Phys. Rev. A **45**, 1371 (1992); R. Friedberg and S. R. Hartmann, Phys. Rev. A **52**, 1601 (1995).

[8] N. W. Carlson, W. R. Babbitt, Y. S. Bai, and T. W. Mossberg, J. Opt. Soc. Am. B, **2**, 908 (1985).

[9] T. W. Mossberg, R. Kachru, and S. R. Hartmann, Phys. Rev. A **20**, 1976 (1979); W. R. Babbitt, *The Response of Inhomogeously Broadened Optical Absorbers to Temporally Complex Light Pulses*, Ph.D. Thesis (Harvard University, Cambridge, Massachusetts, 1987).
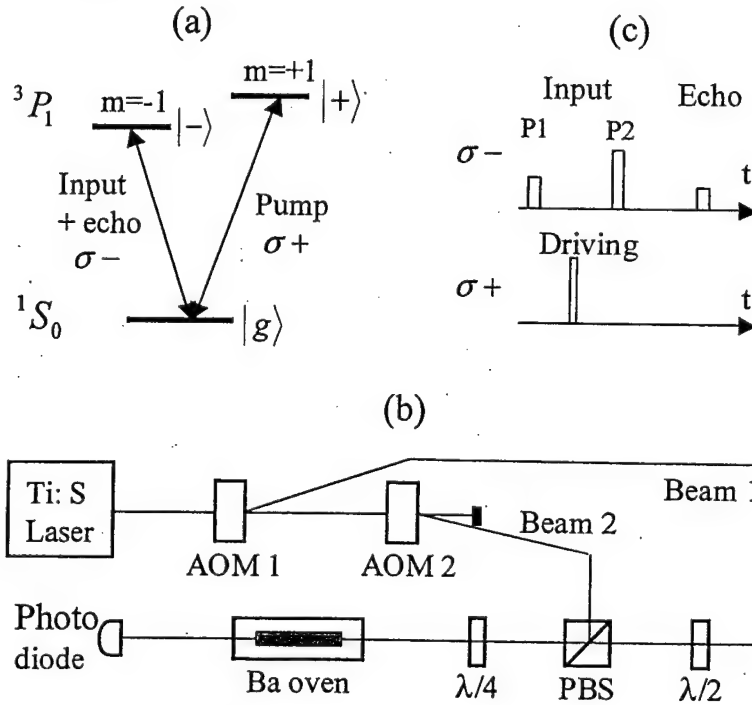
Fig. 9-1 (a). Three-level energy diagram of Barium atom ($^1S_0$ - $^3P_1$ transitions). $^3P_1$ ($m = \pm 1$) is splited by an external magnetic field into a up-shifted level, $|+\rangle$ and a down-shifted level, $|-\rangle$. The $|g\rangle$-$|+\rangle$ and $|g\rangle$-$|-\rangle$ transitions are right-hand ($\sigma+$) and left-hand ($\sigma-$) circularly polarized, respectively. (b). The setup schematic of photon echo experiment. AOM: acoustooptic modulator. PBS: polarized beam splitter. (c) the timing and polarization schemes of the inputs, the driving and the echo pulses. The pulse areas are $\pi/2$, $n\pi$ and π for P1, driving pulse and P2, respectively.
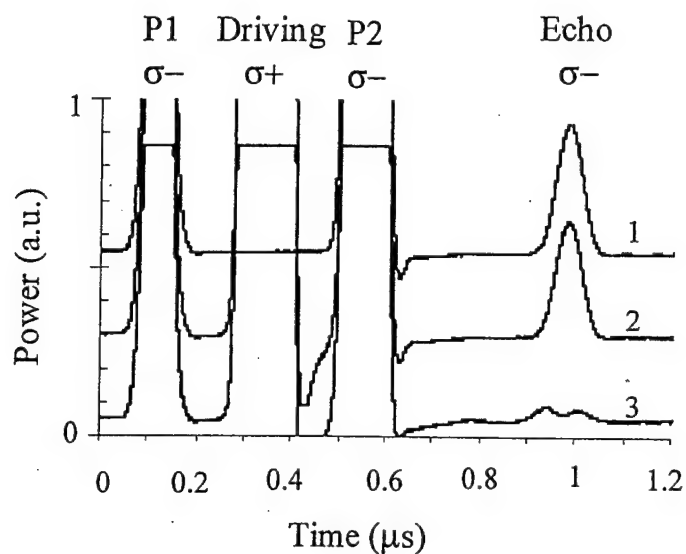
Fig. 9-2. The coupling effect of $^1S_0$ and two $^3P_1$ Zeeman levels in photon echo experiment. The frequency difference between the inputs (pulses 1 and 2) and the driving was 205MHz corresponding to a Zeeman split caused by a 49.4 Gauss magnetic field. Trace 1: echo with magnetic field and without driving pulse, trace 2: driving with π pulse and without a magnetic field, and trace 3: driving with π pulse and the magnetic field.
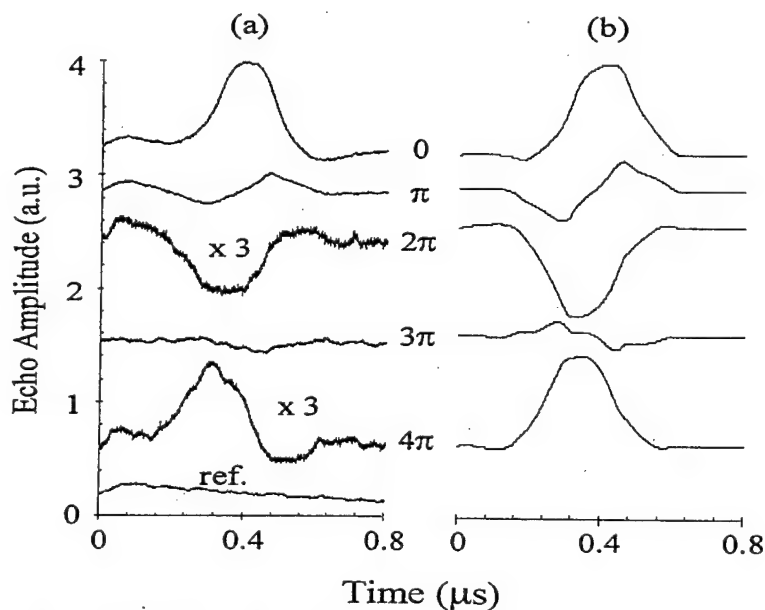

Fig. 9-3 (a). The experimental results of photon echo signals of homodyne detection with various driving pulse areas of 0, π, 2π, 3π and 4π as marked by the traces. The bottom trace: the homodyne reference pulse. (b) The calculated echoes fields under the same condition as those in (a).

Personnel

Personnel Supported

At Montana State University

Wm. Randall Babbitt, Research Assistant Professor, Principal Investigator

Kevin Repasky, Post-Doctoral Research Associate

Kristian D. Merkel, Post-Doctoral Research Associate

Mingzhen Tian, Research Scientist

Zachary Cole, Graduate Research Assistant

Jun Zhao, Graduate Research Assistant

Randy Reibel, Graduate Research Assistant

Joe Fischer, undergraduate

Zeb Barber, undergraduate

At the University of Washington:

Kristian D. Merkel, UW Graduate Research Assistant, working at UW, supported
by AASERT grant from AFOSR. (before he came to MSU for Post-Doc)

Molly J. Byrne, UW Graduate Research Assistant, working at MSU

Carrie S. Cornish, UW Graduate Research Asst., did experimental work at MSU

Collaborations

Leung Tsang, Professor of Electrical Engineering, University of Washington

James Ritcey, Associate Professor of Electrical Engineering, University of
Washington

Rufus L. Cone, Professor of Physics, Montana State University

Todd Harris, Graduate Research Assistant, Montana State University

Publications

Theses supported in whole or in part by the grant

K. D. Merkel, "An optical coherent transient true-time delay device: concept
development and experimental demonstrations including delay programming with
frequency chirped pulses," Ph.D. Thesis, University of Washington, 1998.

Z. Cole, "Atomic coherence-state phase conjugation in optical coherent transients,"
M.Sc. Thesis, Montana State University, 2000.

C. Cornish, "Highly efficient photon echo generation and a study of the energy source
of photon echoes," PhD Thesis, University of Washington, 2000.

R. R. Reibel, "High bandwidth optical coherent transient true-time delay," Ph.D.
Thesis, Montana State University, 2002.

Peer-reviewed journal publications supported in whole or in part by the grant

K. D. Merkel and W. R. Babbitt, "Chirped-pulse programming of optical coherent
transient true-time delays," Optics Letters 23, 528-30 (1998).

W.R. Babbitt and T. W. Mossberg, "Optical waveform processing and routing with structured surface gratings," Optics Comm. 148, 23-26 (1998).

M. Azadeh, C. Sjaarda Cornish, W. R. Babbitt, and L. Tsang , "Efficient photon echoes in optically thick media," Physical Review A 57, 4662-8 (1998).

K.D. Merkel and W. R. Babbitt, "Optical coherent transient continuously programmed continuous processor," Optics Letters, 24, 172-174 (1999).

T.L. Harris, Y. Sun, W.R. Babbitt, R.L. Cone, J.A. Ritcey, and R.W. Equall, "Spatial spectral holographic correlator at 1536nm using 30-symbol quadriphase and binary-phase-shift keyed codes," Optics Letters, 25, 85-7 (2000)

K. D. Merkel, Z. Cole, and W. R. Babbitt, "Signal correlator with programmable variable time delay based on optical coherent transients," J. of Luminescence, 86 375-382 (2000).

C. Sjaarda Cornish, W. R. Babbitt, and L. Tsang " Demonstration of highly efficient photon echoes," Optics Letters 25, 1276-8 (2000).

K. D. Merkel, R. D. Peters, P. B. Sellin, K. S. Repasky and W. R. Babbitt, "Accumulated programming of a complex spectral grating," Optics-Letters 25, 1627-9 (2000).

M. Tian, Z. Barber, T. Chang, R. Reibel, and Wm. R. Babbitt, "Temporal and Spatial Behavior of Photon Echoes Stimulated from Long Pulses", J. Lumin. **98,** 367 (2002).

M. Tian, R. Reibel, Z. Barber and W. R. Babbitt, "Nutational Stimulated Photon Echoes" Opts. Lett. **27,** 1156 (2002)

R. Reibel, Z. Barber, M. Tian and W. R. Babbitt, "Temporally overlapped linear frequency chirped programming for true-time delay amplification," accepted for publication in Optics Letters

M. Tian, R. Reibel, Z. Barber, J. Fischer, and Wm. R. Babbitt, "Observation of geometric phase using photon echoes", Submitted to Physical Review Letters.

Peer-reviewed conference publications supported in whole or in part by the grant
K. D. Merkel and W. R. Babbitt, "Temporal dependence of coherent transient regenerated true-time-delays on intensity of applied pulses," in Conference on Lasers and Electro-Optics, Vol. 6, 1998 OSA Technical Digest Series (Optical Society of America, Washington, DC, 1998) pp 171. San Francisco, Ca., May 3-8, 1998.

C. S. Cornish, M. Azadeh, W. R. Babbitt, and L. Tsang "Efficient waveform recall in absorbing media," in Conference on Lasers and Electro-Optics, Vol. 6, 1998 OSA Technical Digest Series (Optical Society of America, Washington, DC, 1998) pp 214-5. San Francisco, May 3-8, 1998.

K. D. Merkel and W.R. Babbitt, " Optical coherent transient continuously programmed continuous true-time delay processor," in The Ninth Annual DARPA Symposium on Photonic Systems for Antenna Applications (PSAA) session 3. Monterey, CA, February 17-19, 1999

K. D. Merkel and W. R. Babbitt, "Continuously programmed optical coherent transient continuous signal processor" 1999 Optics in Computing OSA Topical Meeting, Snowmass, CO, April 12-16, 1999.

T. L. Harris, Y. Sun, R.L. Cone, W.R. Babbitt, J. A. Ritcey, and R. W. Equall, "A spatial-spectral holographic correlator at 1536 nm using 30-symbol BPSK and QPSK codes optimized for secure communications," 1999 Optics in Computing OSA Topical Meeting, Snowmass, CO, April 12-16, 1999.

T. L. Harris, Y. Sun, R.L. Cone, W.R. Babbitt, J. A. Ritcey, and R. W. Equall, "A spatial-spectral holographic correlator at 1536 nm using 30-symbol BPSK and QPSK codes optimized for secure communications," in Conference on Lasers and Electro-Optics, 1999 OSA Technical Digest Series (OSA, Washington, DC, 1999) pp 282. Baltimore, MD, May 24-28, 1999.

R. L. Cone, Y. Sun, F. Könz, N. M. Strickland, T. L. Harris, C.W. Thiel, T. Böttger, G. Reinemer, W. R. Babbitt, R. W. Equall and R. L. Hutcheson, R. M. Macfarlane, and J. A. Ritcey, " New Rare Earth Materials, Material Concepts, and Demonstrations of Spectral Hole Burning Applications," presented at 6th Int. Meeting of Hole Burning and Related Spectroscopies: Science and Applications (HBRS'99), September 18-23, 1999, Hourtin, France.

K. D. Merkel, K. Repasky, and W. R. Babbitt "Demonstration of a continuously programmed optical coherent transient processor," presented at 6th Int. Meeting of Hole Burning and Related Spectroscopies: Science and Applications (HBRS'99), September 18-23, 1999, Hourtin, France.

M. Tian, Z. Cole, K. D. Merkel, J. Zhao, and W. R. Babbitt "Accumulated Photon Echoes in a Tm3+:YAG Crystal by picosecond pulses," poster presentation at 6th Int. Meeting of Hole Burning and Related Spectroscopies: Science and Applications (HBRS'99), September 18-23, 1999, Hourtin, France.

K. D. Merkel, Z. Cole, and W. R. Babbitt "Programmable variable time delay signal correlator based on six-wave mixing optical coherent transients," poster presentation at 6th Int. Meeting of Hole Burning and Related Spectroscopies: Science and Applications (HBRS'99), Sept. 18-23, 1999, Hourtin, France.

K. D. Merkel, Z. Cole, and W. R. Babbitt, "Signal correlator with programmable variable time delay based on optical coherent transients," IEEE Lasers and Electro-Optics Society 1999 Annual Meeting, p. 566-7, Nov. 8-11, 1999, San Francisco, CA.

C. Sajaarda Cornish, W.R. Babbitt, and L. Tsang,. "Demonstration of highly efficient photon echoes in absorbing media," in Conference on Lasers and Electro-Optics, Technical Digest (Optical Society of America, Washington DC, 2000), pp. 216-217, May 2000, San Francisco, CA.

C. Sajaarda Cornish, L Tsang, and W.R. Babbitt, "A study of the energy source for photon echoes", in Conference on Lasers and Electro-Optics, Technical Digest (Optical Society of America, Washington DC, 2000), p. 491, May 2000, San Francisco, CA.

Z. Cole, K. Merkel, and W.R. Babbitt, "Atomic coherence state phase conjugation in optical coherent transients," in Conference on Lasers and Electro-Optics, Technical Digest (Optical Society of America, Washington DC, 2000), pp.68-69, May 2000, San Francisco, CA.

N. L. Seldomridge, R. Krishna Mohan, W. R. Babbitt and K. D. Merkel, "Steady-state accumulated complex spectral gratings for correlation signal processing" in Conference on Lasers and Electro-Optics, Technical Digest (Optical Society of America, Washington DC, 2001), May 2001, Baltimore, MD.

R. Reibel, Z. Barber, M. Tian, W. R. Babbitt, "Temporally Overlapped Linear Frequency Chirp Programming for True Time Delay Applications," poster, Holeburning, Single Molecules, and Related Spectroscopies, November 18-23, 2001, Taipei, Taiwan.

Z. Barber, M. Tian, R. Reibel, W. R. Babbitt, "Optical Pulse Shaping Using Optical Coherent Transients", CLEO'2002, May 2002, Long Beach, CA.

Interactions/Transitions on research sponsored by this grant
    a. Participation/presentations at meetings, conferences, etc.
       Conference Committees Served on by W. R. Babbitt:
Organizing Committee, Workshop on Applications of Spectral Hole Burning: 1998, March 8-11, 1998, Bozeman, MT.
Program subcommittee member, Wavemixing and Photerefractives, Conference on Lasers and Electro-Optics, May 3-8, 1998, San Francisco, CA. Chaired session on "Advances in Volume Holographic Gratings."
Program committee member, Advanced Optical Memories and Interfaces to Computer Storage, Conference 3468, SPIE Annual Meeting, San Diego, CA, July 22-24, 1998, Chair session on "Protein-Based Memories."
Organizing Committee, Persistent Spectral Hole Burning Workshop 1999, March 7-10, 1999, Bozeman, MT.
Program committee member, 1999 Optics in Computing OSA Topical Meeting, Snowmass, CO, April 12-16, 1999.
Program subcommittee member, Dynamic Holography, Wavemixing, and Photorefractives, Conference on Lasers and Electro-Optics, May 23-28, 1999, Baltimore, MD. Chaired session on Gain Gratings in Laser Media.

Program committee member, Advanced Optical Data Storage: Materials, Systems, and Interfaces to Computers, Conference 3802, SPIE Annual Meeting, July 20-22, 1999 Denver, CO.

Program subcommittee member, Optical Interconnects and Processing Systems, IEEE Lasers and Electro-Optics Society 1999 Annual Meeting, Nov. 8-11, 1999, San Francisco, CA. Chaired Session on Optical Interconnect Circuits and Modelling.

Program subcommittee member, Optoelectronics in Computing: Interconnection, Processing and Data Storage, CLEO Annual Meeting, San Francisco, CA, May 7-12, 2000. Presided at session "Spectral Holography and Novel Concepts."

Program subcommittee member, Optical Interconnects and Processing Systems, IEEE LEOS 2000 Annual Meeting, Rio Grande, Puerto Rico, November 13-16, 2000.

Program subcommittee member, Dynamic Holography, Wavemixing, Photorefractives, and Storage, Conference on Lasers and Electro-Optics, Baltimore, Maryland, May 6-11, 2001.

Chair of program subcommittee, Holography, Wavemixing, Photorefractives, and Storage, Conference on Lasers and Electro-Optics 2002.

Co-organizer, Spectral Holeburning, Single Molecules, and Related Spectroscopies 2003, Bozeman, MT, July 2003.

Invited Conference Presentations related to this grant

W.R. Babbitt, "Memory processing and routing applications of spatial-spectral holography in ultra-high-speed computing systems," Proceedings of the SPIE, Advanced Optical Memories and Interfaces to Computer Storage, San Diego, CA, July 22-24, 1998, Vol. 3468, 304-11 (1998).

W.R. Babbitt, "Multidimensional signal processing with spatio-spectral holography," Proceedings of the SPIE, Advanced Optical Data Storage: Materials, Systems, and Interfaces to Computers, Denver, CO, July 20-22, 1999 Vol. 3802, 164-72 (1999).

W. R. Babbitt, "Optical Coherent Transient Signal Correlators: Science and Applications", 2001 Physics of Quantum Electronics Conference, Snowbird, UT , January 2001.

M. Tian, Z. Barber, T. Chang, R. R. Reibel, and W. R. Babbitt[†] († Invited Speaker), "The Effects of Optical Nutation on Stimulated Photon Echoes," Holeburning, Single Molecules, and Related Spectroscopies, November 18-23, 2001, Taipei, Taiwan.

Peer-reviewed conference presentations:
See above in publications section.

Non-Peer-reviewed conference presentations related to this grant
C. S. Cornish, M. Azadeh, W.R. Babbitt, and L. Tsang, "Efficient waveform recall in absorbing media," Proceedings of the SPIE, Advanced Optical Memories and Interfaces to Computer Storage, San Diego, CA, July 22-24, 1998, Vol. 3468, 174-81 (1998).

W. R. Babbitt, "Hot Gases, Cold Solids, and Smart Pixels for Signal and Image Processing", Proceedings of the 1998 Optical Science and Laser Technology Conference, Bozeman, MT, August 17-18, 1998.

K. D. Merkel, "Optical Coherent Transient True-Time Delays", Proceedings of the 1998 Optical Science and Laser Technology Conference, Bozeman, MT, August 17-18, 1998.

K. Merkel, J. Zhao, K. S. Repasky, and W.R. Babbitt, "Design issues in continuously programmed coherent transient processors," Proceedings of the SPIE, Advanced Optical Data Storage: Materials, Systems, and Interfaces to Computers, Denver, CO, July 20-22, 1999, Vol. 3802, 246-56 (1999).

W. R. Babbitt, "Time-Space Image Processing," Proceedings of the 1999 Optical Science and Laser Technology Conference, Bozeman, MT, August 16-17, 1999.

K. D. Merkel, J. Zhao, and W. R. Babbitt, "Design of a Continuously Programmed Optical Coherent Transient Signal Correlator", Proceedings of the 1999 Optical Science and Laser Technology Conference, Bozeman, MT, August 16-17, 1999.

C. S. Cornish, W.R. Babbitt, and L. Tsang, " A Study of the Energy Source of Stimulated Echoes," poster, Proceedings of the 1999 Optical Science and Laser Technology Conference, Bozeman, MT, August 16-17, 1999.

J. Zhao, K. D. Merkel, and W. R. Babbitt, "Theory of Continuous Programming in Tm3+:YAG," poster, Proceedings of the 1999 Optical Science and Laser Technology Conference, Bozeman, MT, August 16-17, 1999.

M. J. Byrne, W. R. Babbitt, and L. Tsang, "Spectroscopy of Neutron-irradiated Sapphire," poster, Proceedings of the 1999 Optical Science and Laser Technology Conference, Bozeman, MT, August 16-17, 1999.

Z. Cole, K. D. Merkel, and W. R. Babbitt, "Rephasing of Real and Virtual Coherence States," poster, Proceedings of the 1999 Optical Science and Laser Technology Conference, Bozeman, MT, August 16-17, 1999.

Z. Barber, R. Reibel, and W. R. Babbitt, "Applications of Binary Phase Shift Keying for Inhomogeneously Broadened Materials" Optical Science and Laser Technology Conference, Bozeman, Montana, August 14-16, 2000, poster.

K. Merkel, P. B Sellin, R. D. Peters, K. S. Pepasky and W. R. Babbitt, "Accumulated Complex Spectral Gratings Using a Frequency Stabilized Laser," Optical Science and Laser Technology Conference, Bozeman, Montana, August 14-16, 2000.

Z. Barber, R. Reibel, M. Tian, W. R. Babbitt, "Application of Phase Modulated Optical Signals to Inhomogeneously Broadened Materials," poster, American Physical Society Annual Meeting, March 11, 2001, Seattle, WA.

Workshop presentations:

C. S. Cornish, M. Azadeh, W. R. Babbitt, and L. Tsang "Highly Efficient Waveform Recall in Absorbing Media", poster, Workshop on Applications of Spectral Hole Burning: 1998, Bozeman, MT, March 8-11, 1998

K. D. Merkel, K. Repasky, and W. R. Babbitt, "Demonstration of a continuously programmed optical coherent transient true-time-delay device," Persistent Spectral Holeburning Workshop 1999, March 7-10, 1999, Bozeman, MT.

T. L. Harris, Y. Sun, R. L. Cone, W. R. Babbitt, J. A. Ritcey, R. W. Equall, and R. L. Hutcheson, "A spatial-spectral holographic correlator at 1536nm using 30-symbol BPSK and QPSK codes optimized for secure communications," poster, Persistent Spectral Holeburning Workshop 1999, March 7-10, 1999, Bozeman, MT.

C. Sjaarda Cornish, W. R. Babbitt, and L. Tsang, "Experimental Demonstration of Highly Efficient Photon Echoes in an Absorbing Medium." Workshop on Applications of Spectral Hole Burning 2000, Big Sky, Montana, July 9-12, 2000.

K. D. Merkel, P. B. Sellin, R. D. Peters, K. S. Repasky and W. R. Babbitt, "Accumulated Complex Spectral Gratings using a Frequency Stabilized Laser," Workshop on Applications of Spectral Hole Burning 2000, Big Sky, Montana, July 9-12, 2000.

R. Reibel, M. Tian, and W. R. Babbitt, "Optical Nutations on Three Pulse Accumulated Photon Echoes," Workshop on Applications of Spectral Hole Burning 2000, Big Sky, Montana, July 9-12, 2000, poster.

Honors/Awards
   W. R. Babbitt, Special Invention Award, The Boeing Company, 1998
   W. R. Babbitt, Charles and Nora L. Wiley Faculty Award for Meritorious Research, MSU, 2002
   Z. W. Barber, Goldwater Scholarship for excellence in science and math, 2002

New Discoveries, Inventions, and patent disclosures
   K. D. Merkel and W. R. Babbitt, " Coherent Transient Continuously Programmed Continuous Processor (CPCP)," Patent Filed December 22, 1999.